FINAL REPORT

NASA CONTRACT NAS8-39716

TEMPERATURE DEPENDENCE OF DIFFUSIVITIES IN LIQUID ELEMENTS (LMD)

Period of Performance
2/3/93 through 5/31/98

Principle Investigators

R. MICHAEL BANISH

FRANZ ROSENBERGER (Retired)

Center for Microgravity and Materials Research
University of Alabama in Huntsville
Huntsville, Alabama 35899

Table of Contents

INTRODUCTION

This report is a summary of the work performed under NASA grant NAS8-39716 (Liquid Metal Diffusion). This research was to advance the understanding of diffusion mechanisms in liquid metals and alloys through accurate diffusivity measurements over a wide range of temperatures, including the proximity of the materials melting points. Specifically, it was driven towards developing a methodology (and subsequent flight hardware) to enable several diffusion coefficient measurements (i.e., at several different temperatures) to be performed using a *single* sample.

The Liquid Metal Diffusion (LMD) was funded as a Flight Definition Project in February 1993 in response to NRA 91-OSSA-20 (Microgravity Science and Applications Division). The Science Concept Review for LMD was held during April 1994. In January 1995 we were informed that we had failed this review and the project was change to ground-based activities only. A new proposal was submitted for the next NRA addressing the panels concerns.

As part of NASA's Risk Mitigation program, a scaled-down version of the hardware was funded in July of 1995 for a flight opportunity utilizing experiment on the Microgravity Isolation Mount. This experiment was to determine the self-diffusivity of indium at 185°C. The LMD was transferred to the Mir Space Station in STS-81 and returned on STS-84 (January - May 1997). Three, out of five, self-diffusion data sets were returned. A description of this experiment/hardware is included below.

This summary is only intended to give the reader an overview of the results obtained for the tasks outlined in the original proposal. Research that was not published is explained in more detail. At the end of this report is a list of refereed publications and invited talks that were given as a result of this work. The reader is directed to these for further details.

Background

The diffusion of species in liquids governs numerous materials preparation processes of technological importance. In particular, a detailed understanding of diffusion in liquid metals and alloys is pivotal for the interpretation of various phenomena encountered in metallurgical and semiconductor manufacturing processes. Transport experiments in gases and crystalline solids can readily be designed to yield diffusion coefficients with great accuracy at normal gravity [1]. In liquids, however, such measurements are hampered by uncontrollable and significant contributions from convection.

Simple scaling illustrates the difficulty of obtaining purely diffusive transport in liquids: In a system with a diffusivity of 10^{-5} cm^2/s and a characteristic diffusion distance of about 1 cm, the diffusion velocity is of the order of 10^{-5} cm/s. If true diffusion is to be observed, convective contributions to mass transport must be small compared to the diffusion fluxes. Therefore, convection velocities parallel to the concentration gradient must be of order 10^{-7} cm/s (10 Å/sec !) or less. Hence, the results of diffusion experiments in liquids tend to be contaminated by buoyancy-driven flows.

As a consequence, the standard deviations of liquid diffusivity data obtained on Earth range typically from several 10% to several 100% [2]. This high uncertainty is particularly deplorable since, due to the complex structures of liquids and, thus, the lack of realistic structure models, our theoretical understanding of diffusion in liquids is very limited. There are currently various

theoretical models for the temperature dependence of diffusivities in liquids. The predictions range from a pure Arrhenius-type behavior (exponential increase with temperature) to combinations of Arrhenius laws with power laws and pure power laws [2,3]. However, due to the large scatter of existing liquid diffusivity data, it is currently not possible to adequately evaluate these theories. Thus, accurate liquid diffusion data are needed to provide guidance in the development of both fundamental diffusion theory and transport models essential for materials processing.

Efforts to exclude convective transport contributions in diffusion experiments by using narrow capillaries have revealed contamination of the results by (poorly understood) wall effects [4, and references in 2]. It appears as if, in analogy to surface and interface diffusion in solids, depending on the materials involved, lower or higher diffusion fluxes exist in a thin layer at the container wall. This effect sets lower limits to the useful capillary diameter. Thus, the drastic reduction of buoyancy-driven convection under low gravity conditions provides a promising means of studying true diffusion in liquids.

Objectives and Tasks

Within this framework the following technological and scientific objectives were proposed:

- Development of a technique for dynamic *in-situ* measurements of diffusivities and their temperature dependence in melts, with much higher efficiency than current (one sample/one data point) approaches permit.
- Development of a flight-certified hardware package (GAS container) to perform such diffusivity measurements automatically, with relatively high flight frequency.
- Establishment of a large definitive database for the temperature dependence of self-diffusivities in liquid metals and alloys, in order to further the development of the theory of diffusion in liquids and our understanding of numerous diffusion processes underlying materials processing.
- Exploration of the possibility to approximate low gravity diffusion conditions in conducting liquids on Earth through the application of magnetic fields.

WORK PERFORMED UNDER THIS CONTRACT

Measurement Methodology (task 1)

The experimental methods for diffusivity measurements can be grouped into *direct* or tracer techniques, and *indirect* or probe techniques [3,5,6]. The direct techniques employ radioactive or stable isotopes and diffusivities are deduced from Fick's laws. In the indirect methods, some relaxation parameter associated with the macroscopic transport process is determined, from which the macroscopic diffusivities are deduced through model considerations. Due to this limitation we chose to apply a direct technique for the measurement of self-diffusivities.

There are several *direct* techniques for the determination of diffusivities. They include the capillary-reservoir, long capillary or diffusion couple, the shear cell and the diaphragm cell techniques. In all of these techniques, diffusion coefficients are typically obtained by heating the diffusion couple through the melting point to the specified temperature, holding the sample for a define period of time, and then quenching the sample. The diffusant concentration is determined throughout the sample, and the diffusivity calculated from these concentration versus distance values.

This approach is both inefficient, yielding only one data point per sample, and prone to *additional* convective contaminations [see below] of the data due to the melting, and subsequent, freezing of the sample. Therefore, a primary goal of this project was to develop an in-situ, real-time, i.e., a radiotracer, measurement technique that would allow several diffusivity points to be determined in a single sample. Note that this requires being able to calculate the diffusivity from an arbitrary starting profile, not only a "stepped" starting profile.

Early methodology investigations

We planned to employ a more "traditional" algorithm using 15-30 detectors along the length of the sample to monitor the concentration distribution. The initially solid, cylindrical sample contains a radioactive isotope at one end. After melting, radiation escaping through small bores in an isothermal liner/radiation shield is monitored via a chain of detectors. The diffusivities would then be determined from the temporal records of evolving concentration profiles through measurements of radioactive tracer emission. Diffusivity data could be gathered over a range of temperatures in a single experiment.

Utilizing the different radiation absorption behavior of different photon energies, we could also investigate the significance of the "wall" effect. This effect is believed to contaminate diffusion studies in narrow capillaries used to suppress convection at normal gravity.

In this approach, no radiation is received from the very ends of the diffusion sample. In addition, several consecutive profiles are determined at a given temperature. .Then the temperature is changed, and the recording of consecutive profiles resumed; etc. Hence, an algorithm was needed that does not require data from the diffusion cell boundaries and is not limited to specialized initial conditions (such as a step function):

Starting from an initial arbitrary concentration profile C(z), Fick's second law

$$C_z(z,t) = DC_{zz}(z,t) \qquad (1)$$

is solved for the diffusivity, in the interval a→b such that $0 < a < b < L$, with L the length of the diffusion cell.

Define an arbitrary function f(z) that meets the following restrictions:

$$f_z(a) = f_z(b) = 0 \qquad (2)$$

Thus, by integrating over n consecutive concentration profiles (using a third order spline to the discrete data) D is obtained for any initial conditions and without use of the physical boundary conditions.

Extensive numerical modelling was performed using a variety of f(z)'s and concentration profiles. When using ideal (temporal) concentration profiles the input diffusivity was always recovered within a few 0.1%. However, on applying more realistic uncertainties (1-3 standard deviations) to the concentration data the uncertainty in the resulting diffusivity was greater than 10%. These results were independent of the number of detectors used (10-30)

Therefore, this "traditional" approach was abandoned and a two detector approach initially used by Codastefano, Zanza, and DiRusso [7] was tested.

Codastefano methodology

Codastefano et al., showed that the higher order terms in the Fourier expansion of the diffusion equation canceled and the remaining one were small (compared to the first two) when the two detectors were *maintained* at L/6 from each end of the sample, i.e.,

$$z_1 = L/6 \text{ and } z_2 = 5L/6 \, . \tag{3}$$

see fig 1a. Then, under these conditions, the diffusivity D can be determined "directly" from the slope of the count difference versus time,

$$\ln[n_1(t) - n_2(t)] = \text{constant} - (\pi/L)^2 D\, t \, , \tag{4}$$

where L is the sample length at the measurement temperature $n_1(t)$ and $n_2(t)$ are the total counts (over a given time) at measurement time t. The intensities n_1 and n_2 are assumed to be proportional to the concentrations C_1 and C_2, respectively. The characteristic shape of the signal traces $n_1(t)$ and $n_2(t)$ associated with the spreading of the diffusant is plotted in Fig. 1b. Obviously, before the first measurement, $C_0(z)$ must have spread enough to provide a significant signal at both detector locations.

The concept underlying our setup was originally developed for diffusivity measurements with gaseous krypton. In these experiments the overall cell length was fixed; thus maintaining a single L. Measuring diffusivities in liquid samples over a (wide) temperature range with a single sample the overall sample length L, of course, changes throughout the experiment. Thus, for our application of this technique, additional detectors are required to maintain the advantageous L/6 and 5L/6 measurement locations However, we found two pairs of collimation bores and detectors are sufficient. They are positioned such that, taking into account the thermal expansion of the sample, support structure and radiation shield, one pair fulfills condition (1) at the lowest measurement temperature and the other pair at the highest. As a consequence, for all intermediate temperatures, there is always a collimation bore above and below the exact positions required. (Note that the size and fixed position of the detectors are chosen such that most of the radiation emanating from a "moving" collimator remains detected).

For the corrections we assume that A and B, respectively, are the diffusant concentrations at the collimator positions z^- and z^+ which bracket the concentration C at the accurate measurement position z_m defined by Eq. 3. Then, noting that, at the stage where sufficient signal is obtained at the second collimators, the curvature of the concentration profile is small, we approximate the C at x_m by the linear interpolation

$$C = \left(\frac{z^+ - z_m}{z^+ - z^-}\right) A + \left(\frac{z_m - z^-}{z^+ - z^-}\right) B \, . \tag{5}$$

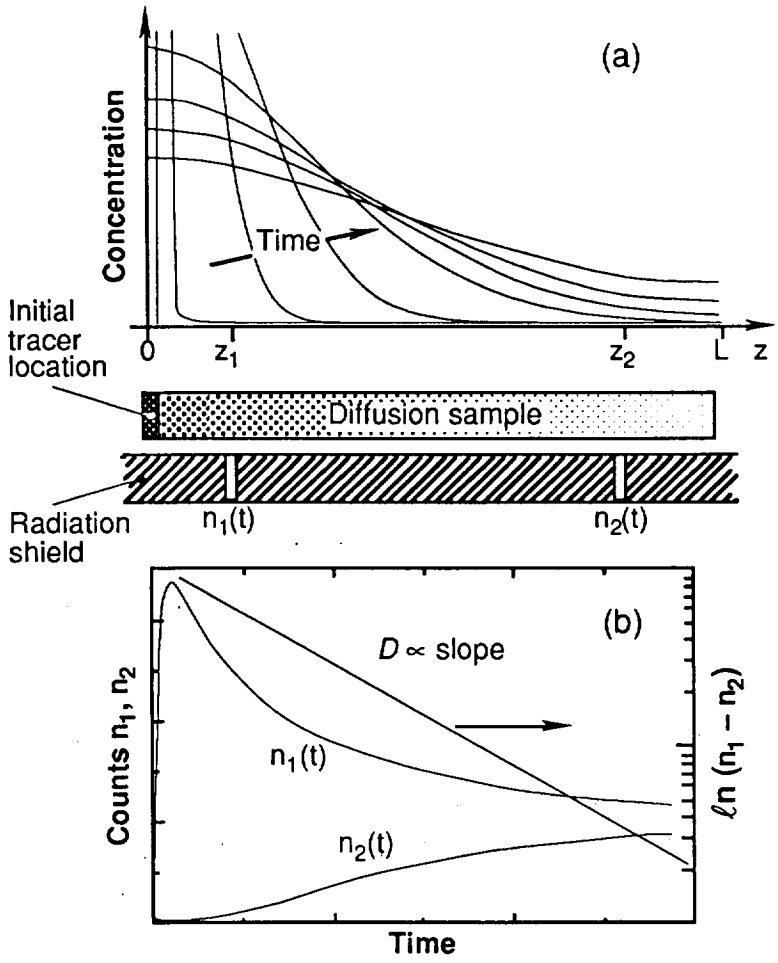

Fig. 1. (a) Schematic presentation of the evolution of the concentration profile and location of the measurement locations. (b) Timetraces of the signals at the two measurements locations, and corresponding presentation of the signal difference according to Eq. (2).

Extensive numerical computations showed that this methodology is very robust. The input diffusivity could be recovered to with a few) 0.1% even with ± 2 standard deviations on the input concentration (count rate) data.

Hardware Design and Construction (task 2)

Choice of radiation detectors

Since the experimental hardware developed for this project would be flown in a spacecraft the initial requirements for the radiation detectors were:

- operational with cooling only to room temperature,

• a sufficiently high absorption coefficient, for the photons of interest, such that no more than 1 cm of material would be necessary,

• spectral resolution of better than 5 keV,

• low energy pedestal of no more than 15-20 keV

These requirements "limited" us to using either solid state detectors (i.e., CdTe, HgI_2, Si) or inorganic scintillators such as Tl-doped NaI or CsI. Silicon was rejected because of its low absorption coefficient and low spectral resolution. We therefore tested the following materials, high-pressure bridgman-CdTe, Cl-doped CdTe, CdZnTe, high-pressure bridgman CdZnTe, HgI_2, and Tl-doped CsI. In order to test for the full range of photon energies (both high and low) that we could use in our self-diffusion studies these materials were tested with I^{129} (30, 40 and 65 keV photon energy) Cd^{109} (22 and 88 keV), Am ^{241} (60 keV) and Se^{75} (121, 136, 264, 280, and 400 keV). The selection criteria between the various detectors were the peak to valley ratios, the full-width at half-max (FWHM) to the peak height, location of the low-energy pedestal, and the spectral resolution. These materials were tested at room temperature up to 65 °C.

Based on the above selection criteria, CdZnTe was selected as the detector material. As a supplier we chose eV Products, Inc. (Saxonburg, PA) which had done (and continues to do) extensive work in miniaturizing the detector circuitry and noise reduction.

Diffusion sample and ampoule

The considerations for the optimum length of the diffusion couple for a Codastefano based methodology is different than for long capillary technique cells. In the Codastefano technique the diffusivity is determined from the signal difference between the two (L/6 and 5L/6) detector locations. Also, before valid measurements can begin, both the initial maximum "wave" of diffusant must pass the first detector and a (statically) significant signal level must be present at the second, far, detector. Thus, there is an optimal sample, and diffusant, length, such that measurements are valid shortly after the maximum wave has passed the first detector and such that the diffusant concentration is equalibrated (fully diffused) over a long enough time to allow for multiple determinations. In addition, the sample diameter is optimized to allow for a reasonable (radioisotope) activation parameter, i.e., if the isotopically enriched portion is too small, a much long activation time is required. Finally, the sample diameter should be large enough to allow us to investigate the "wall effect". Following extensive numerical modelling we found that a 3 mm ϕ sample with a 29 mm long native abundance section and a 1 mm radioactive tracer (diffusant) portion sufficiently fulfilled the criteria.

Then, as indicated in Fig. 1a, we use an initially solid cylindrical diffusion sample which consists mostly of inactive material (solvent) and a short section of activated isotope, as the diffusant, located at one end. After melting of the sample and heating to a uniform measurement temperature T, the evolution of the diffusant concentration distribution $C(z)$ is monitored through the intensity of the radiation received through two bores (collimators) in a radiation shield.

BN Ampoule design

The BN ampoule consists of four pieces and a graphite spring, see figure 2. The four pieces are the ampoule body, bottom plug, plunger and screwcap, which are constructed from Carborundum grade AX05. This high-purity grade BN is not wet by any of the metals under consideration for this work. The ampoule body I.D. is reamed to 3.00, with tolerances of -0 and +

0.01 mm to minimize errors in the (total) sample length. The ampoule body O.D. varies depending on the wall thickness of the particular outer cartridge. The bottom plug is precision machined to 3.05 ± 0.02 ϕ and 5.0 ± 0.02 mm long. It is press fitted into the body, providing "square" corners at the sample bottom. The plunger is individually fit to less than 0.02 mm clearance to the ampoule body. Close tolerance between the plunger and the ampoule bore prevents liquid metal from escaping. The low-force graphite spring pressing against the plunger

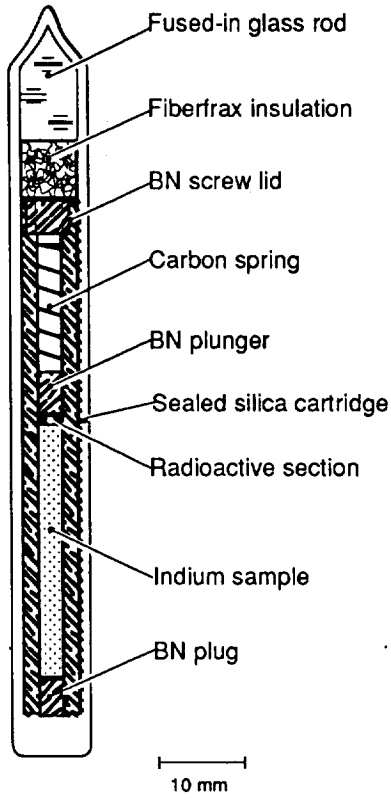

Fig. 2. Cross-section of diffusion sample cartridge.

ensures a flat interface at both ends of the sample. This ampoule is vacuum-baked at high temperature to remove gaseous contaminants.

An outer cartridge provides a vacuum or gas seal to minimize oxidation or transport of the diffusion couple. The specific material used varies depending on the temperature range and radiotracer employed. Up to the present time, silica glass, aluminum and stainless steel have been used for these cartridges.

Sample preparation

The native abundance section is prepared from 6N starting material. It is vacuum-cast (10^{-6} mm Hg) in a 2.9 mm diameter BN mold to remove residual oxides, voids and gaseous contaminates. It is then removed, trimmed and weighted to 0.1 mg. This section is then loaded into the diffusion ampoule itself and vacuum cast again to approximately 100 °C above the planned processing temperature. The final vacuum casting minimizes any voids and residual oxide in the material.

The isotopically enriched (diffusant) section is prepared into a flat disk using a boron nitride ampoule consisting of three parts machined to tight tolerances. After loading and assembling the ampoule the isotopically enriched material is vacuum melted, again to approximately 100 °C above the planned experiment temperature. It is then removed under inert gas, weighted to 0.1 mg and sealed in a silica glass tube for neutron activation. The activated section is removed from the silica tube, under inert gas, and loaded into the ampoule. After replacing the plunger and spring the BN ampoule is mechanically closed with the screw lid and inserted into the (square-bottomed) outer cartridge.

Isothermal liner / radiation shield

The Isothermal liner/radiation shield was to function as both a zone leveler, to minimize any temperature nonuniformities across and along the diffusion sample, and as a collimator for the emitted photons. As originally conceived LMD was to be flown as an "shuttle-independent" GAS cannister experiment. Thus, both experiment mass and the power required for operation were to be minimized. Gold was chosen as the liner/shield material due to its high thermal conductivity, high radiation absorption and ready machinability. The initial liner/shield design yielded a cylinder approximately 21 mm diameter (7 mm wall) and 90 mm long. Sixteen 0.67 mm collimators were bored in a spiral pattern along the liner/shield axis. In order to minimize heat transfer, and therefore, the input power required, considerable effort was devoted to reducing the convective and radiative heat transfer. As presented at the LMD Science Concept Review (SCR) the liner/shield was suspended by a wire "spokes". A series of gold-flashed thermal shields minimized the radiative losses. With this design we were able to maintain sample temperatures of 800 °C with 20 watts. Assuming 28 V power (or batteries) this represented a current draw of less than 1 A.

However, in the first diffusion measurements with radiotracers excessive background through the shield overwhelmed the signal (radiation) from the collimators. Thus, it was obvious that either the shield wall thickness was not sufficient or that the collimation hole diameter was too small; or both.

A series of experiments was run to determine the optimum collimator geometry. Both the collimation bore diameter and the shield thickness were varied, between 1 and 3 mm, and 13 to 39 mm of Pb, respectively. A small collimation bore diameter gives high spatial resolution but a low signal-to-background level; for a large collimation hole the converse is true. A thin shield thickness (low bore length) has minimum scatter in the bore but high direct radiation penetration and fluorescence. The results of these tests indicated that a 2 mm diameter collimation hole and a 16 mm bore length would provide the optimum signal-to-background level for diffusion measurements. Thus, the gold liner/shield that has been used for all measurements to date under this contract has been 41 mm diameter, with an approximately 9 mm center bore (see below), 70 mm long. 2 mm diameter collimation holes are bored through the liner/shield at the required L/6 and 5L/6 positions.

Choice of Radioisotopes to be Used (task 3)

As stated above, an original objective of the LMD project was to development a measurement methodology and flight hardware. Beyond suggesting individual elements or alloys for investigation little justification was given for specific choices. The Science Concept Review panel found this to be scientifically unsound. In response to this criticism, in preparation for submitting to the next available NRA, we systematically searched the literature for possible liquid structure

features that may be responsible for specific diffusion mechanisms. From this we selected a series of elements for study based on their "class-like" self-diffusion behavior.

Class-like self-diffusion behavior of molten elements

In spite of the large uncertainties in diffusivity data, enough insight has been obtained, in particular through a few measurements spanning wide temperature ranges, to recognize some class-like behavior that can be associated with temperature-dependent structure features of liquids. D(T) data are conveniently tabulated in terms of the two parameters D_0 and Q in the relation $D = D_0 \exp(-Q/RT)$, where Q is understood only as an apparent "activation energy", without the intent to support activated state theories. Such compilations of data, and corresponding plots of *ln* D vs. 1/T readily reveal a few cases of clear "non-Arrhenius" behavior, i.e. discontinuous, steep increases of the diffusivity with temperature.

Tin, for instance, shows a sharp increase of D with rising T around 1030 °C [8]. This has been associated with the dissociation of a second structure in the liquid [8]; see below. This dissociation is indicated by the disappearance of a subsidiary peak in plots of the scattered X-ray intensity versus scattering vector [9] and the appearance of a peak in the differential thermal analysis curve [10]. Similarly, in liquid *gallium*, below 70 °C the Arrhenius plot yields a diffusion "activation energy" of 1.1 kcal/mol, while at higher temperatures it is about twice this value [11]. Correspondingly, a subsidiary X-ray peak disappears at around 100 °C [12]. *Mercury* shows a similar behavior, with the disappearance of the second liquid structure and the sudden increase in D(T) occurring at around 0°C [10]. Liquid *tellurium*, the only elemental liquid semiconductor (see also [13]), on the other hand, possesses a sharp decrease in the slope of D(T) with increasing temperature around 500 °C, i.e. 50 °C above the melting point [14]. Again, neutron scattering data suggest a structural transition around this temperature [15]. The initial steep slope in D(T) has been interpreted in terms of the dissociation of chain-like structures and, thus, increased thermal mobility of molecules in liquid tellurium, that is essentially completed around 500 °C [14]. In contrast to these complex systems, the alkali metals as well as copper and silver show rather monotonic D(T) behavior [3].

The above cases suggest that for liquid elements for which detailed diffraction and, thus, structure data exist, valuable predictions of the D(T) can be made. Such structure data exist for a large number of liquid metals and semimetals [16-18]. Most simple liquids and liquid metals exhibit a *sharp* main peak in plots of scattered intensity versus scattering vector. Liquid metals exhibiting a *symmetrical* sharp maximum (Saweda type-a) include the alkali metals, Mg through Ba, copper, silver, gold and the transition metals. Symmetrical main peaks, which are also obtained from hard-sphere-interaction diffraction models [18], indicate complete randomness in atom arrangement, i.e. no preferred configuration of atoms, however transient [16].

In several liquid metals, the first scattering peak is asymmetrical (Saweda type-b [18]), and in some cases has a pronounced shoulder on the high-angle (lower atomic distance) side of the peak (Saweda type-c). This group includes, in addition to *Sn, Ga* and *Hg* mentioned above, *Zn, Cd, Si, Ge, Sb,* and *Bi,* with possible minor asymmetries in the peaks of *In* [19] and *Tl* [20]. Note that both *Ge* and *Si*, which are semiconductors in the solid state, turn metallic on melting [13]. In the non-metallic liquids *Se* and *Te*, which show predominantly covalent (homopolar) bonding, this subsidiary peak is particularly pronounced. Thus the probability of finding an asymmetric maximum is higher in elements of the higher groups, in which the solid-state bonding is predominantly non-metallic [21]. The distance values corresponding to these subsidiary peaks

often represents the nearest-neighbor distance characteristic of the covalent bond in the solid state, e.g. gray tin in the Sn-system, while the main peak closely correspond to the distance in the metallically-bonded solid, e.g. white tin. This suggests that in these liquids there is a short-term localization of valence electrons in bound states between pairs or groups of neighboring atoms within an otherwise completely random metallically bonded matrix. With increasing temperature, the formation of short-lived clusters becomes less likely, leading to the disappearance of the subsidiary diffraction peaks. Even more pronounced than in *Se* and *Te*, liquid *sulfur* (an insulator) shows on heating several structural transitions, between various molecular ring and chain configurations, over a range of more than 100 °C above the melting point [22,10]

High/Low energy photons for "wall effect" investigations

In addition to its real-time feature, this isotopic labeling technique permits investigations of the perceived "wall effect" mentioned above. By employing an isotope which emits photons at two sufficiently different energies and, thus, different self-absorption behavior, transport in the bulk of the sample and near the container wall can be distinguished to some extent. For example, based on attenuation data, for the 24 keV and 190 keV photons of ^{114m}In [23] we have calculated the fraction of the total radiation received at the two different emission energies outside a 3 mm thick sample *vs.* the distance of the emitter from the surface of the sample; for details of the one-dimensional slab model used see Refs.[24]. Note that the 24 keV photons received are predicted to originate in essence only from a 300 μm deep surface layer. The 190 keV photons, on the other hand, stem from throughout the whole sample slab. This behavior was experimentally confirmed, for details see Jalbert, Banish, and Rosenberger at the end of this report. Thus, in selecting elements for self-diffusion studies consideration was given to isotopes that emitted (multiple) photons both high enough in energy to be representative of "bulk" diffusion and low enough to represent transport in the "wall" region of the sample.

Systems to be used in diffusivity measurements

Based on the above considerations we proposed investigating the following systems.

- Simple liquids:

  Indium which may show some weak nonmonotonic behavior, has a combination of low and high energy photons that can be utilized for quantifying wall effects, a conveniently low melting point and a wide liquid temperature range.

  Rubidium has been studied over approximately 80% of its liquid state. However, the temperature dependence of Rb has been reported as both T^2 and Arrhenius.

  Aluminum based on neutron diffraction data aluminum is expected to have a monotonic temperature dependence. However, aluminum self-diffusivity values are not available.

- Complex liquids:

  Cadmium has two advantageous photons for studying bulk and wall transport.

  Gallium with low melting point and wide liquid range with x-ray diffraction data showing a pronounced asymmetry in the first peak.

  Tin which has been extensively investigated on Earth and to some extent in space [2,8,9], producing controversial results. It also has two particularly advantageous photons for studying bulk and wall transport.

Tellurium and *selenium*, which should provide interesting features in D(T), due to the multiple structures that are known to exist in their liquid states. *Te* has the advantage of two distinctly different energy photons and *Se* that of a lower melting point. Note that the energies of *Te* also appear well suited for wall effect investigations.

Convective Effects on Diffusivity Measurements (task 4)

Numerical modelling of magnetic fields to suppress convection

The scaling considerations presented above show that convection velocities in typical self-diffusion experiments must be reduced to much less than 10^{-5} cm^{-1}. In principle, this can be achieved in liquid metals using a steady magnetic field to damp the flow. In order to assess the magnitude of the field required, we have computed buoyancy-driven flows in a model diffusion cell geometry with and without applied magnetic field.

The 2D Navier-Stokes-Boussinesq equations were solved for flow driven by small lateral temperature gradients in a vertical cavity of 5 cm length with a width of 1 and 3 mm, respectively. As illustrated in Fig. 1, two types of lateral temperature boundary conditions were considered. In case 1, a uniform temperature difference of either 0.1 or 0.01 K was applied across the slot. In case 2, a "cold spot" of about 0.1 K was assumed at the upper right corner. Transverse and vertical magnetic fields were considered and it was assumed that generation of secondary magnetic fields by the flow could be neglected. The two-dimensionality of the problem allowed us to neglect the electric field [25].

The steady Navier-Stokes Boussinesq equations governing the transport of heat, mass and momentum are written in dimensionless form as

$$\frac{\partial \mathbf{u}}{\partial t} + \mathbf{u}\cdot\nabla\mathbf{u} = -\nabla p + Pr\nabla^2\mathbf{u} - RaPr\theta\mathbf{k} - Ha^2\,(\mathbf{u}\times\mathbf{B})\times\mathbf{B}, \qquad (6)$$

$$\nabla\cdot\mathbf{u} = 0 \qquad (7)$$

and

$$\frac{\partial \theta}{\partial t} + \mathbf{u}\cdot\nabla\theta = \nabla^2\theta, \qquad (8)$$

where $\mathbf{u}(\mathbf{x},t)$, $\mathbf{B}$ and $\theta(\mathbf{x},t)$ are the dimensionless velocity, magnetic field and temperature, respectively, and $Ra = \beta g\Delta T d^3/\kappa\nu$, $Pr = \nu/\kappa$ and $Ha = Bd(\sigma/\mu)^{1/2}$. The physical properties β, ΔT, d, κ, σ, μ and ν are, respectively, the thermal expansion coefficient, the maximum deviation from the desired uniform temperature, the width of the slot, the thermal diffusivity, the electric conductivity, and the dynamic and the kinematic viscosity. Ra, Pr and Ha are the Rayleigh, Prandtl and Hartmann numbers, respectively.

The governing equations were recast in stream function vorticity form and discretized using a Chebyshev pseudospectral collocation method with an Adams-Bashforth/second backward Euler temporal scheme [26,27]. The discretized problem was solved using an influence matrix method [26-28]. It is well known that at high values of the Ha the flow is confined to narrow boundary layers with thickness proportional to $Ha^{-1/2}$ for walls perpendicular to the field lines and Ha^{-1} for walls parallel to the field lines [25]. Thus, we needed to ensure sufficient spatial resolution to

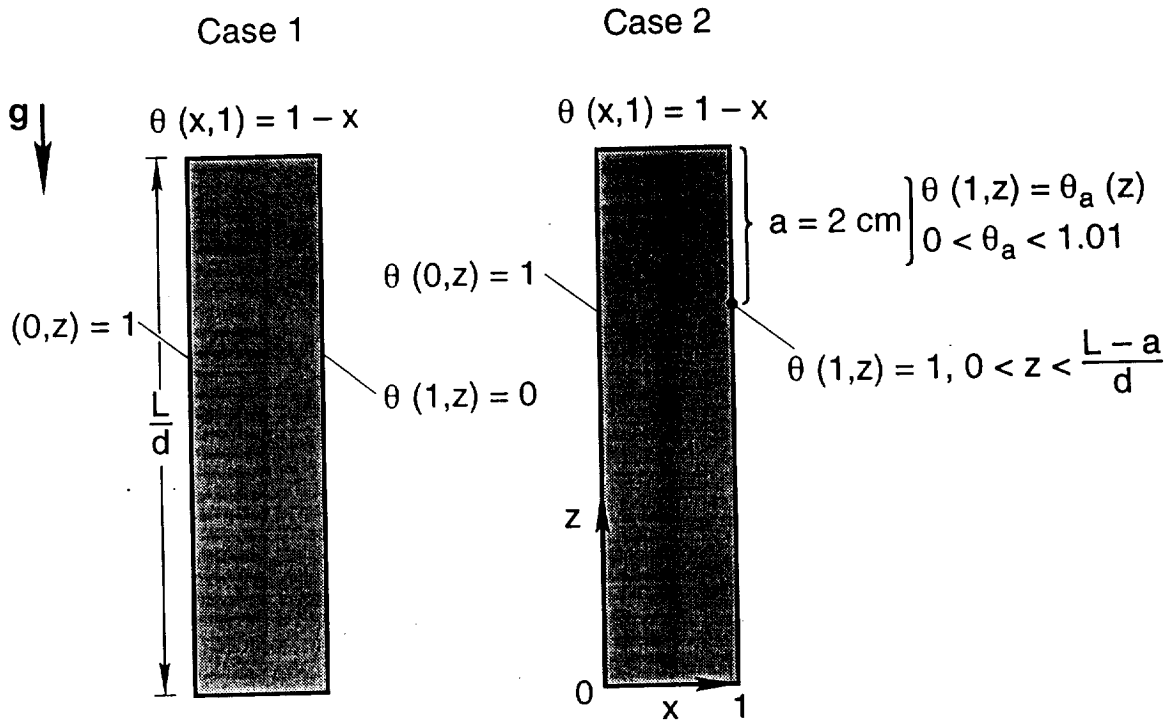

Figure. 3. Sketch of problem domain for both case 1 (lateral temperature gradient extends throughout the domain) and case 2 (lateral temperature gradient on the right-hand wall only extends over 2 cm).

capture the boundary layers. Collocated Chebyshev polynomials[1] were distributed such that for N+1 points in a given coordinate direction $x_i = \cos(i\pi/N)$, i = 0,1..., N. We used 33×85 collocation points. This gave us 6 points inside 1.225 mm for the horizontal boundary layers (for the 3 mm cell width) and 6 points inside 0.477 mm for the vertical boundary layers. Given that the points are more closely spaced as one approaches the boundary, this appears to provide sufficient resolution for these flows.

Using the physical properties of liquid tin, we obtained solutions for both temperature boundary conditions. The lateral magnetic fields were found to be the most effective for damping the flow. This is because the main damping effect is on the velocity component perpendicular to the field lines. In the absence of a magnetic field, the maximum velocity is the vertical component, w. A vertical field is not as effective in reducing the w-velocity since it only directly damps the u-component. Nevertheless, in the bulk of the domain, flow velocities are diminished and the flow is squeezed close to the boundaries. Three sets of results for lateral fields are presented in Table 1. For case 1, both cell widths were considered. Since for case 2, the 3 mm width velocities at high Hartmann numbers were similar in magnitude to those in case 1 we did not carry out calculations for 1 mm widths for this case. The flow velocities obtained in the absence of a magnetic field are

[1] The Chebyshev polynomials are defined as $T_n(x) = \cos(n \arccos x)$, n = 0,1,..., and $-1 \le x \le 1$.

about the same as those predicted by the approximation of Batchelor [29], i.e. ~ 10^{-2}Raκ/d. For Ha = 0 the calculated results scale linearly with a decrease in temperature or with gravity level.

Summary

We have calculated the convective flow in diffusion cells arising from small horizontal temperature gradients with and without steady, transverse magnetic fields. Only for high fields, on the order of 1 Tesla, could velocities be brought down to the order of 10^{-5} cm s^{-1} or less. At high lateral fields the maximum velocity is the horizontal component, which is typically twice the vertical maximum. Since typical diffusive speeds will be on the order of 10^{-5} cm s^{-1} (based on v~ D/L, where D is the diffusivity and L= 5 cm), it appears that, even for lateral temperature nonuniformities as low as 0.01 K, unless a combination of thin capillaries (less than 1 mm width) and large magnetic fields (in excess of 1 Tesla) are used, the maximum flow speeds cannot be reduced significantly below diffusive speeds.

Table 1: Convection speeds in diffusion cell model with and without transverse magnetic field.

Case 1		B [T]	Maximum velocity (3 mm) [cm s^{-1}]		B [T]	Maximum velocity (1 mm) [cm s^{-1}]	
ΔT = 0.1K	Ha		u	w		u	w
	0	0	1.13×10^{-2}	1.87×10^{-2}	0	1.23×10^{-3}	2.08×10^{-3}
	10	0.1	3.26×10^{-3}	6.57×10^{-3}	0.29	3.62×10^{-4}	3.84×10^{-4}
	50	0.5	6.5×10^{-4}	1.3×10^{-4}	1.47	3.32×10^{-5}	2.32×10^{-5}
	100	1	1.29×10^{-4}	5.01×10^{-5}	2.95	1.25×10^{-5}	6.09×10^{-6}
	147	1.47	7.60×10^{-5}	2.63×10^{-5}			
ΔT = 0.01K							
	0	0	1.13×10^{-3}	1.87×10^{-3}	0	1.23×10^{-3}	2.08×10^{-3}
	10	0.1			0.29	3.52×10^{-5}	3.838×10^{-5}
	50	0.5	3.63×10^{-5}	2.07×10^{-5}	1.47	3.33×10^{-6}	2.31×10^{-6}
	100	1			2.95	1.24×10^{-6}	6.098×10^{-7}
	147	1.47	7.61×10^{-6}	2.63×10^{-6}			
Case 2 ΔT = 0.1K							
	0	0	7.83×10^{-3}	9.73×10^{-3}			
	10	0.1	2.61×10^{-3}	2.3910^{-4}			
	50	0.5	3.25×10^{-4}	1.77×10^{-4}			
	100	1	1.21×10^{-4}	4.88×10^{-5}			

Numerical modelling of buoyancy-driven convection in diffusion cells

To provide more quantitative guidance for experimental work, we numerically modeled diffusive-convective transport in vertical cylinders. The dimensions of the cylinders were chosen to correspond to typical diffusion experiment geometries. Thermal boundary conditions with slight asymmetries were imposed to simulate small deviations from isothermality. Since the objective is to simulate convective effects on self-diffusion, the diffusant and sample were assumed to have the same mass density. The three-dimensional time-dependent transport of the diffusant (initially located at one end of the sample) was simulated for the physical properties of liquid indium.

The liquid phase was assumed to be a Boussinesq fluid contained in a closed vertical circular cylinder of length L and diameter 2R. Gravity acts along the cylinder axis. The temperature at the vertical wall of the cylinder has the form: $T(r,\theta,z) = (T_1 - T_2)/2 - (T_1 + T_2)(\cos\theta)/2 + \Delta T_z z/L$. Here $T_1 - T_2$ is the maximum lateral temperature difference across the cylinder at any height z, and ΔT_z is the temperature difference between the bottom and the top. The temperature of the latter are $T(r, \theta, 0) = (T_1 - T_2)/2 - (T1 + T2)\ r\ (\cos\theta)/2R$ and $T(r, \theta, L) = T(r, \theta, 0) + \Delta T_z$, respectively, The governing equations for the time-dependent transport of heat and momentum in the system were solved using finite difference on an equally spaced mesh and on a variably spaced mesh using the code CFD2000 which is based on the finite volume method.

Summary

The simulation yielded various results of practical consequence. We found that, even for temperature nonuniformities $T_1 - T_2$ as low as 0.1 °C, convective transport in capillaries of 1 mm diameter can largely exceed diffusion. Furthermore, the convective contribution to transport may be increased by "stabilizing" ΔT_z's. Hence, the widely used approach of keeping the top of diffusion samples slightly warmer than the bottom appears to be a dubious means of "preventing convection". Most striking, we found that diffusive-convective transport can result in profiles of the radially averaged concentration values that are analytically indistinguishable from pure diffusion profiles. This finding casts considerable doubt on various geometrical criteria previously used to demonstrate the absence of significant convective contamination diffusivity data plots. In summary, reduced gravity conditions are essential for definitive diffusivity measurements in liquid phases of macroscopic dimensions. For details of this work see (Alexander, Ramus and Rosenberger).

Risk Mitigation Flight Opportunity

A simpler version Liquid Metal Diffusion experiment was selected for a flight opportunity under the NASA/Mir Glovebox/MIM risk mitigation program. The scientific and technological goals of this phase were:

- Determination of the effects of steady residual gravity and g-jitter aboard spacecraft on liquid diffusivity measurements.
- Determination of the influence of g-level on possible "wall effects".
- Test of anchoring technology to prevent void/bubble formation in liquid metal diffusion samples at low gravity.
- Tests of a sample exchange technique for multiple runs of a diffusivity measurement setup during a spaceflight.
- Test of radiation detector performance with respect to space background radiation level and sample activity requirements.

The LMD hardware utilized the (Canadian Space Agency) Microgravity Isolation Mount (MIM) as part of the Mir Space Station. The MIM hardware provided a unique opportunity for testing the effects of residual gravity and g-jitter on liquid diffusion sample. It provided for vibration isolation *and* defined g-inputs up to 10^{-3} g_0; as well its' latched configuration; where g-gitter and residual accelerations would be transmitted to the samples.

To take full advantage of the MIM capabilities, five ^{114m}In/In metal self-diffusion samples were flown. All samples were to be processed at 185 °C. (Note, initially the samples were to be processed at 200 °C. However, because of concerns from the Russian Space Agency, the processing temperature was decreased to 185 °C) The operating characteristics of the MIM during sample processing were to be:

- One sample with the MIM latched down,
- two samples with isolation only,
- one sample with 10^{-3} to 10^{-2} g_0 pulses, at approximately 0.01 Hz, normal to the sample axis,
- one sample with 10^{-3} to 10^{-2} g_0 pulses, 0.01 Hz, perpendicular to the sample axis.

The design and construction of the flight hardware employed the same systems and technology used for ground-based experiments. Containment and electronic redundancy requirements that were placed on the hardware did not change its functionality. Additional samples were contained in a hand operated storage carousel not typically used on the ground. Figure 4 is a scaled cross-section of the flight hardware indicating the major components.

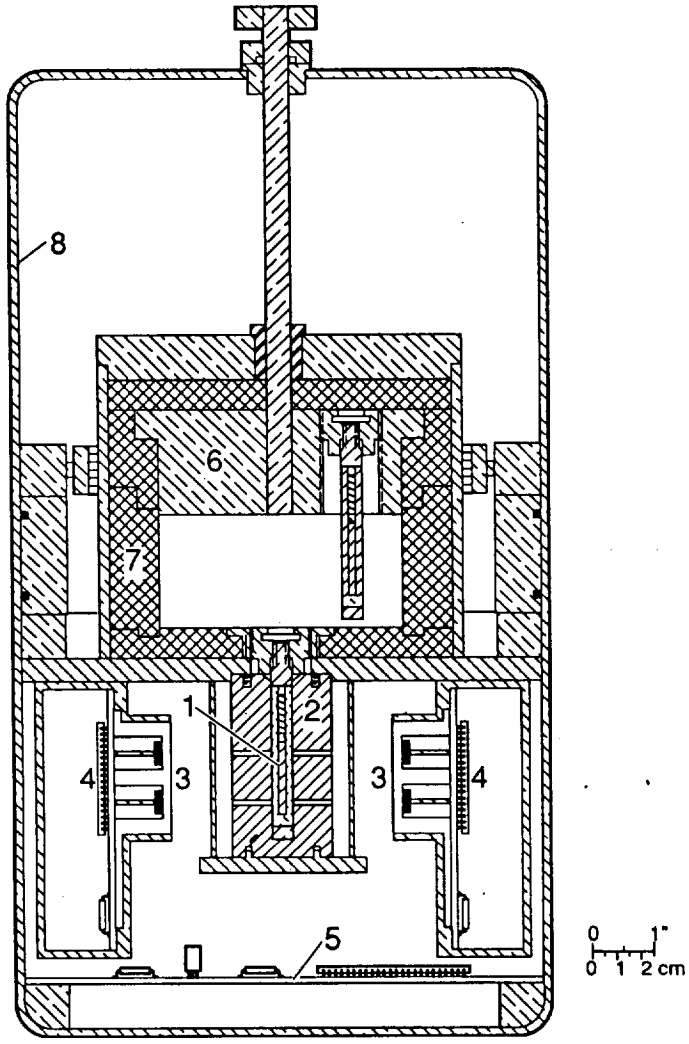

Figure. 4. Liquid metal diffusion apparatus cross-section: (1) diffusion sample in cartridge, (2) heated isothermal liner/radiation shield, (3) CdZnTe detector pairs, (4) preamplifiers/energy discriminators, (5) circuit board, (6) carousel with four additional sample cartridges, (7) lead pig, (8) sealed aluminum housing.

Application of technique to indium: ground-based and low-gravity results

Indium was chosen as the first element for investigation due to its:

- low melting point of 156 °C,
- high boiling point of approximately 2000 °C, thus, giving a very wide liquid range,
- radioisotope having low (24 keV) and high (190 keV) photons with a high enough branching ratio such that activation was relatively straight forward. The energy range of these photons was such that wall effects could be investigated.

Diffusivity determinations were performed at a single temperature as a verification of the method and hardware, both on Earth and aboard the space station Mir. In the ground-based tests

we also investigated the effect of the initial source activity levels on the signal-to-noise ratio. All experiments were run until diffusant/emitter uniformity was obtained throughout the sample. Typically this requires 100 hours at the low temperatures used in these experiments.

The first five ground-based runs were performed at temperatures near 200 °C. In these early experiments the temperature control with a manually adjusted DC power supply was not optimal. Indium samples with room temperature lengths of 30 mm and different initial source thicknesses and activities were used. Radiation counts were taken continuously and summed every 10 seconds. Diffusant source parameters and apparent diffusivity results are summarized in Table 2.

Table 2. Summary of ground-based results at 200 °C.

Source activity [μCi]	Self-diffusivities in indium [10^{-5} cm^2/s] Left detectors 190 keV	Left detectors 24 keV	Right detectors 190 keV	Right detectors 24 keV
53	2.44±0.16	(3.74)*	(only one pair used)	
75	2.60±0.17	2.47±0.16	2.64±0.17	2.43±0.16
150	2.46±0.16	(3.69)*	2.46±0.16	(2.36)*
600	2.14±0.14	2.16±0.14	2.21±0.14	2.24±0.14
5000	2.33±0.15	2.04±0.13	2.24±0.14	2.06±0.13

* ground loop/stray capacitance problems: calibration shifts during experiment.

After a thorough examination of the raw data and calculated diffusivities an initial activity of 1 mCi was chosen as sufficient for single temperature measurements. Using this activity, samples were prepared for the liquid element diffusion (LMD) experiments on space station Mir

Four of the five diffusion samples delivered to Mir were run. Data from three tests were returned. Data from the second sample was lost due to software problems; the fifth sample was not run due to Mir time constraints, i.e., defined input g-pulse runs were not carried out. Therefore, instead of the MIM operating conditions stated above two samples were run in latched mode, i.e., without g-jitter isolation, samples 1 and 3. Run 2 was performed with active isolation. Table 1 shows our low temperature (approx. 200 °C) indium self-diffusivity values both at normal and low-gravity (less than 10^{-4} - 10^{-6} g_0).

Table 3. LMD Mir results.

Run	Temperature [° C]	Self-diffusivities in indium [10^{-5} cm^2/s] Left detectors 190 keV	Left detectors 24 keV	Right detectors 190 keV	Right detectors 24 keV
1(latched)	186.5 ± 0.8	1.99±0.13	2.07±0.13	1.98±0.13	2.06±0.13
2(isolated)	185.0 ± 0.4	2.09±0.13	1.98±0.13	2.07±0.13	*
3(latched)	186.5 ± 0.4	2.08±0.13	2.09±0.13	2.05±0.13	*

* ground loop/stray capacitance problems: calibration shifts during experiment.

Discussion of low temperature results

The average (normal gravity) values of the self-diffusivity of In^{114m}/In at 185 °C are;

- 2.22 ± 0.159 (for 190 keV photons) and,
- 2.11 ± 0.154 x 10^{-5} cm^2/sec, (for 24 keV photons),

(The normal gravity values in Table 21 were corrected to 185 °C by the factor 1 x 10^{-7} $cm^2/sec/K$.)

The average, low-gravity, indium self-diffusivity values are;

- 2.04 ± 0.047 (for 190 keV photons) and,
- 2.04 ± 0.044 x 10^{-5} cm^2/sec (24 keV photons).

These low temperature experiments established that this technique and hardware will provide accurate diffusivity data in element liquids. Several aspects are noteworthy. First, within the experimental uncertainty, the results are reproducible. Furthermore, the agreement between the left and right detector pairs, see Tables 2 and 3, indicates that at these low temperatures either convective transport contributions are insignificant or, less likely, affect the concentration distribution in the measurement plane rather symmetrically. The latter could result from a convection roll that is oriented normal to the plane of measurement. The reduced spread of the low-gravity data, while the D_i's themselves are not that different, are difficult to unambiguously explain. Similar results have been noted by other authors [30]. While, there may be some convective contributions (in the ground based data) to the apparent diffusivity, they are probably nonsteady and, therefore, difficult to characterize fully, or eliminate.

Given the low scatter and reproducibility of the reduced-gravity data we report these values with good confidence. Therefore, we do not see a need to measure these values again. The reproducibility between the isolating and latched runs indicates, coupled with our numerical modelling, that the LMD cell was isothermal to better than 0.1°C, which was a design goal.

Overall, these results are on the low end of the range of published values for D_{In}(200°C) which are from (2.2 - 3.8) × 10^{-5} cm^2/s. Finally, it should be noted that for all data, transport in the bulk of the sample and near the container wall were indistinguishable, i.e., no 'wall effect' was detected.

Risk Mitigation Results

The overall results from this flight opportunity were very positive and for most aspects the experiment was a success. In addition to the low temperature indium self-diffusivity results:

1) the sample exchange and positioning mechanism worked properly,

2) the radiation detectors worked well within specifications,

3) the chosen sample activity was acceptable for the (Mir) background radiation environment, and

4) the sample containment/restraint system work properly.

Summary

During the course of this work, most of the proposed objectives were successfully completed. We did not pass our Science Concept Review and, therefore, we did not build and fly hardware capable of measuring diffusivities of several elements over a wide temperature range. However, we did develop a methodology for this that has been demonstrated on the ground over a wide temperature range. This same Codastefano methodology was successfully used for our low temperature spaceflight results. Hardware components, radiation detectors, isothermal liner/shield, etc., were also developed during this project. Numerical modelling showing the extreme sensitivity of diffusion measurements to convective contaminations was completed. Finally, numerical modelling of the self-defeating nature of magnetic fields to suppress convective contaminations, ***in diffusivity measurements***, was also completed.

References

[1] P. J. Dunlop, B. J. Steel and J.E. Lane, in *Physical Methods of Chemistry*, ed. by A. Weissberger and B. W. Rossiter (Wiley, New York 1972) Vol. I, Part IV, p. 205-349.

[2] G. Frohberg, in *Materials Sciences in Space*, ed. by B. Feuerbacher, H. Hamacher and R. J. Naumann (Springer, Berlin 1986) [a] p.93-128 and [b] 425-446.

[3] M. Shimoji and T. Itami, *Atomic Transport in Liquid Metals* (Trans Tech Publications, Aedermansdorf, Switzerland 1986).

[4] G. Careri, A. Paoletti and M. Vincentini, Nuovo Cimento **X**, 4050 (19580.

[5] N.H. Nachtrieb, Berichte Bunsenges. 80, 678 (1976).

[6] N.H. Nachtrieb, Self-diffusion in liquid metals, in *Proceed. Internat. Conf. on Properties in Liquid Metals* (Taylor and Francis, London, 1967) edited by Adams, Davies and Epstein, p. 309.

[7] P. Codastefano, A. Di Russo and V. Zanza, Rev. Sci. Instrum. **48,** 1650 (1977).

[8] J.P. Foster and R.J. Reynik, Met. Transact. **4**, 207 (1973).

[9] K. Furukawa, B.R. Orton, J. Hamor and G.I. Williams, Phil. Mag. **8,** 141 (1963).

[10] J.P. Foster, C. Daniels and R.J Reynik, Met. Trans. **6A**, 1294 (1975).

[11] S. Larsson and A. Lodding, in *Diffusion Processes*, ed. by J.N. Sherwood et al. (Gordon and Breach, N.Y. 1971) vol. 1, p.87.

[12] A.H. Norten, J. Chem Phys. **56**, 1185 (1972).

[13] J.E. Enderby, in Amorphous and Liquid Semiconductors, edited by J. Tauc (Plenum, New York, 1974) Chpt. 7.

[14] D.H. Kurlat, C. Potard and P. Hicter, Phys. Chem. Liqu. **4**, 183 (1974).

[15] F. Friedel and G. Cabane, J. Physique **32**, 73 (1971).

[16] J.R. Wilson, Met. Rev. **10**, 381 (1965).

[17] W.H. Young, Can. J. Phys. 65, 241 (1987).

[18] Y. Waseda, *The Structure of Non-crystalline Materials* (McGraw-Hill, New York, 1980).

[19] H. Ocken and C.N.J. Wagner, Phys. Rev. **149**, 122 (1966).

[20] N.C. Halder and C.N.J. Wagner, J. Chem Phys. **45**, 482 (1966).

[21] W. Hume-Rothery and G.V. Raynor, *Structure of Metals and Alloys* (XX, London 1962).

[22] F.A. Cotton and G. Wilkinson, *Advanced Inorganic Chemistry*, Third Edition (Interscience, New York, 1972) p. 425.

[23] W.H. Tait, *Radiation Detection* (Butterworths, London 1980).

[24] Tsoulfanidis,N., *Measurement and Detection of Radiation*, (McGraw-Hill, Washington, 1983).

[25] T. Alboussiere, J.P. Garandet and R. Moreau, Buoyancy-driven convection with a uniform magnetic field. Part 1 Asymptotic analysis, J. Fluid Mechanics, **253** (1993) 545.

[26] J.I.D. Alexander, S. Amiroudine, J. Ouazzani and F. Rosenberger, Analysis of the low gravity tolerance of Bridgman-Stockbarger crystal growth II: Transient and periodic acceleration, J. Crystal Growth **113** (1990) 21.

[27] J.M. Vanel, R. Peyret and P. Bontoux, A pseudo-spectral solution of vorticity stream function equations using the influence matrix technique, in *Numerical Methods for Fluid Dynamics II*, K.W. Morton and M.J. Baines, eds. (Clarendon Press, Oxford, 1986) 463.

[28] J.P. Pulicani, A spectral multi-domain method for the solution of 1D Helmholtz and Stokes type equations, Computers and Fluids **16** (1988) 207.

[29] G.K. Batchelor, Heat transfer by free convection across a closed cavity between vertical boundaries at different temperatures, Q. J. Appl. Math. **7** (1953) 209.

[30] Smith, R. W. and Zhu, X., Materials Science Forum, **215-216**, 113 (1996).

Papers published and submitted for publication

L.B. Jalbert, R.M. Banish and F. Rosenberger, *Real-time Diffusivity Measurements in Liquids at Several Temperatures with one Sample,* Phys. Rev. E 57 (1998) 1727.

L.B. Jalbert, F. Rosenberger and R.M. Banish, *On the Sensitivity of Liquid Diffusivity Measurements to Deviations from 1-D Diffusion,* J. Phys.: Cond. Matter 10 (1988) 1.

R.M. Banish, L.B. Jalbert, and F. Rosenberger, *Self-diffusivity Measurements in Liquid Indium at 185°C on the Mir Space Station,* in preparation for publication in Microgravity Science and Technology.

J.I.D. Alexander, J-F. Ramus and F.Rosenberger, *Numerical simulations of the convective contamination of diffusivity measurements in liquids,* Microgravity Sci. and Tech. 9 (1996) 158.

Invited Presentation

Self-diffusion in Liquid Elements, Institut fur Werkstoffe and Verarbeitung, Technische Universitat Munchen, Garching, 2 February 1998.

Numerical Simulation of the Convective Contamination of Diffusivity Measurements in Liquids, Royal Institute of Technology, Stockholm, Sweden, 10 June, 1997.

On the Convective Contamination of diffusivity Measurements in Liquids, Joint Xth European and Vith Russian Symposium on Physical Sciences in Microgravity, St Petersburg, Russia, 15-21 June 1997.

Real-time Radiotracer Diffusion Measurement Technique, Royal Institute of Technology, Stockholm, Sweden, 13 June, 1997.

Real-time Radiotracer Diffusion Measurement Technique, Spacebound 97, May 11-14, Montreal, Canada.

On the Convective Contamination of diffusivity Measurements in Liquids, Spacebound 97, May 11-14, Montreal, Canada.

Materials Science in Mircogravity, Festkolloquium fur Professor Langbein, ZARM, Bremen, 14 February, 1997.

Real-time Radiotracer Diffusion Measurement Technique, 35th Aerospace Sciences Meeting, Reno, NV January 6-9, 1997

On the Convective Contamination of diffusivity Measurements in Liquids, 35th Aerospace Sciences Meeting, Reno, NV January 6-9, 1997

Real-time Radiotracer Diffusion Measurement Technique, 31th COSPAR Scientific Assembly, Birmingham, England, July 18-24, 1996

Real-time Radiotracer Diffusion Measurement Technique, 31th SPIE Meeting, Denver, CO, July 8-12, 1997

PHYSICAL REVIEW E VOLUME 57, NUMBER 2 FEBRUARY 1998

Real-time diffusivity measurements in liquids at several temperatures with one sample

Lyle B. Jalbert, R. Michael Banish, and Franz Rosenberger
Center for Microgravity and Materials Research, University of Alabama in Huntsville, Huntsville, Alabama 35899
(Received 25 September 1997)

Based on the methodology of Codastefano, Di Russo, and Zanza [Rev. Sci. Instrum. **48**, 1650 (1977)], we have developed a technique for the *in situ* measurement of diffusivities in liquids at several temperatures with one sample. In this approach, which circumvents solidification of the diffusion sample prior to concentration profiling, the evolution of the concentration distribution of a radiotracer is followed in real time using two pairs of radiation detectors. A detailed description of the experiment setup and its optimization by computer simulations is given. In experiments with ^{114m}In/In, apparent self-diffusivities were obtained between 300 °C and 900 °C with an uncertainty of ±5%. By utilizing the different self-absorption characteristics of the 24- and 190-keV photons of ^{114m}In, transport in the bulk of the sample and near the container wall was investigated independently. No difference was found. [S1063-651X(98)09002-3]

PACS number(s): 66.10.Cb, 07.85.−m, 07.05.Fb

I. INTRODUCTION

Most techniques to measure diffusion in high-temperature liquids involve solidification of the sample before concentration profiling [1–3]. Inevitable nonuniformities during freezing can introduce considerable concentration redistribution due to segregation [3]. Furthermore, in samples of low thermal conductivity, the heat of solidification can lead to significant temperature nonuniformities. As a result, convective mixing and a higher apparent diffusivity can result even in systems that are perfectly isothermal *during* the liquid diffusion process [3].

Some radial concentration nonuniformities observed in samples that were solidified in diffusion capillaries have been assigned to "wall effects" [4]. These effects are perceived, in analogy to surface and grain boundary diffusion, to originate from different diffusion rates near solid walls and in the bulk liquid. However, as pointed out by Nachtrieb [3], the range of true wall effects should be limited to a few atomic dimensions from the wall. This is corroborated by analytical investigations in terms of particle density wave scattering by a wall [5] as well as by molecular-dynamics simulations [6,7]. Both approaches suggest that true wall effects should be limited to some 50 Å from the wall, i.e., to such a small fraction of the sample cross section that they should be undetectable by macroscopic diffusivity measurements.

We have addressed the above problems and developed an experimental technique for real-time measurements of diffusivities in liquids. This radiotracer technique circumvents solidification of the diffusion sample prior to concentration profiling. Furthermore, by employing an isotope that emits photons at (two) sufficiently different energies, transport in the bulk of the sample and near the container wall can be distinguished. In the following, we will present the conceptual considerations underlying this technique, simulations carried out towards its optimization, details of the experimental setup and sample preparation, and applications to self-diffusivity measurements in liquid indium.

II. EXPERIMENT CONCEPT

A. Methodology

The concept underlying our setup was originally developed by Codastefano, Di Russo, and Zanza for diffusivity measurements with gaseous krypton [8]. As schematically indicated in Fig. 1(a), we use an initially solid cylindrical diffusion sample that consists mostly of inactive material (solvent) and a short section of activated isotope, as the diffusant, located at one end. After melting of the sample and heating to a uniform measurement temperature T, the evolution of the diffusant concentration distribution $C(z)$ is monitored through the intensity of the radiation received through

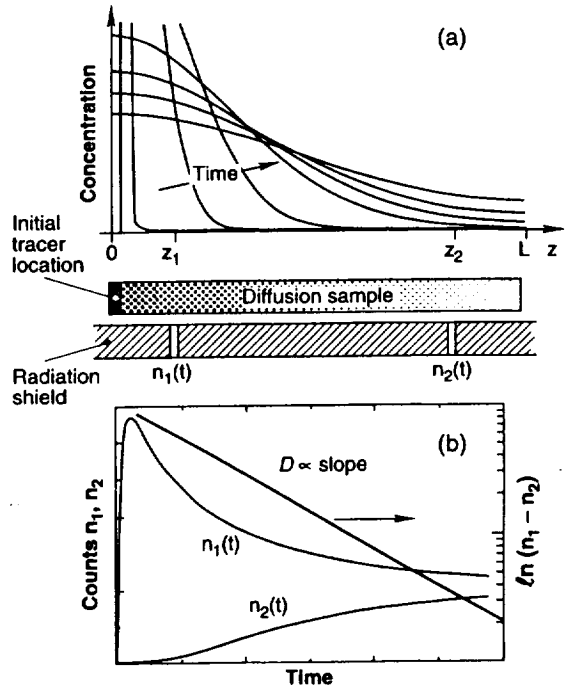

FIG. 1. (a) Schematic presentation of the evolution of the concentration profile and location of the measurement locations. (b) Time traces of the signals at the two measurements locations, and corresponding presentation of the signal difference according to Eq. (2).

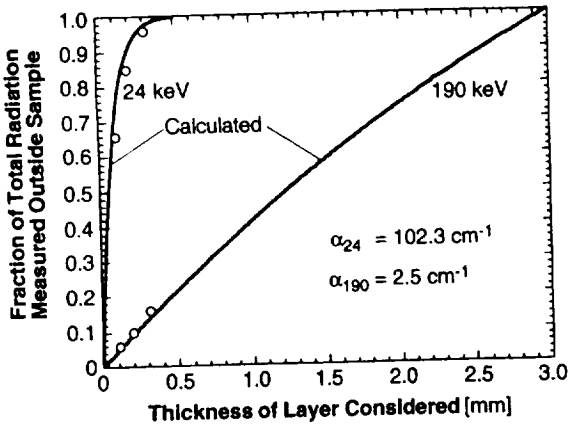

FIG. 2. Emission of 24- and 190-keV photons from 3-mm-thick indium sample containing ^{114m}In versus distance of the emitting atoms from the sample surface.

two bores (collimators) in a radiation shield. These intensities n_1 and n_2 are assumed to be proportional to the concentrations C_1 and C_2, respectively. The characteristic shape of the signal traces $n_1(t)$ and $n_2(t)$ associated with the spreading of the diffusant is plotted in Fig. 1(b).

To satisfy the requirements of the algorithm used to evaluate the diffusivity [8], the radiation collimation bores must be positioned at

$$z_1 = L/6, \quad z_2 = 5L/6, \tag{1}$$

where L is the sample length at the measurement temperature. The diffusivity D is then calculated from the difference of the signal traces using the relation

$$\ln[n_1(t) - n_2(t)] = \text{const} - (\pi/L)^2 Dt, \tag{2}$$

where the constant depends on the concentration profile $C_0(z)$ at the beginning of the measurement. Since the $C_0(z)$ does not explicitly enter the D evaluation, diffusivities can be consecutively determined at several temperatures during the spreading of the concentration profile in the same sample. Obviously, before the first measurement, $C_0(z)$ must have spread enough to provide a significant signal at both detector locations.

In addition to its real-time feature, an isotopic labeling technique permits investigations of the perceived "wall effect" mentioned in the Introduction. By employing an isotope that emits photons at two sufficiently different energies and thus different self-absorption behavior, transport in the bulk of the sample and near the container wall can be distinguished to some extent. Figure 2 illustrates this approach. Based on the attenuation data for 24- and 190-keV photons of ^{114m}In [9], we have calculated the fraction of the total radiation received at the two different emission energies outside a 3-mm-thick sample vs the distance of the emitter from the surface of the sample; for details of the one-dimensional slab model used see Refs. [10,11]. Note that the 24-keV photons received are predicted to originate in essence only from a 300-μm-deep surface layer. The 190-keV photons, on the other hand, stem from throughout the whole sample slab. Thus, using an appropriate detector circuit with energy discrimination capability (see Sec. IV C), transport near the wall of the sample container and in the sample bulk can be distinguished to some extent.

We have experimentally confirmed the above selective absorption behavior. Indium disks of 100, 200, and 300 μm thickness were prepared from indium that had been uniformly diffusion doped with ^{114m}In. The normalized ratios of the 24- and 190-keV counts received from these disks agreed well with the predicted values; see the data points on the curves in Fig. 2.

B. Collimator positions and thermal expansion

Relation (2) is based on the specific location requirement for the detectors given by Eq. (1) with respect to the sample length L. For applications of this measurement technique at several temperatures with one sample, corrections are required to account for thermally induced changes in sample dimension and collimator locations. For these corrections it is advantageous to use two pairs of collimation bores and detectors. They are positioned such that, taking into account the thermal expansion of the sample, support structure, and radiation shield, one pair fulfills condition (1) at the lowest measurement temperature and the other pair at the highest. As a consequence, for all intermediate temperatures, there is always a collimation bore above and below the exact positions required. (Note that the size and fixed position of the detectors is chosen such that most of the radiation emanating from a "moving" collimator remains detected; see also Sec. IV B).

For the corrections we assume that A and B, respectively, are the diffusant concentrations at the collimator positions z^- and z^+ that bracket the concentration C at the accurate measurement position z_m defined by Eq. (1). Then, noting that, at the stage where sufficient signal is obtained at the second collimators, the curvature of the concentration profile is small, we approximate the C at z_m by the linear interpolation

$$C = \left(\frac{z^+ - z_m}{z^+ - z^-}\right) A + \left(\frac{z_m - z^-}{z^+ - z^-}\right) B. \tag{3}$$

III. EXPERIMENT SIMULATION AND OPTIMIZATION

We have carried out detailed computer simulations to optimize the experiment setup with respect to sample size and activity, measurement accuracy, and number of $D(T)$ data obtainable with one sample. In the following we derive the basic relations used; for more details on the simulations the reader is referred to Ref. [10].

A. Evolution of concentration distributions including sample expansion

In a realistic simulation of the experiments, changes in sample length due to thermal expansion during heating to the first measurement temperature and heating or cooling to consecutive temperatures must be taken into account. Let the initial concentration profile in the sample of total length L_1 at temperature T_1 be

$$g(z) = C_0 \theta(z - l_i), \quad 0 < z < L_1, \tag{4}$$

with C_0 the initial concentration over the initial length of the activated section l_i and $\theta(z - l_i)$ a step function equal to 1 for $z < l_i$ and 0 for $z > l_i$. With this initial condition and the closed-system boundary condition

$$C_z(0,t)=C_z(L_1,t)=0, \quad 0<t, \tag{5}$$

assuming that the diffusivity D is independent of concentration and coordinate z, one obtains from Fick's second law

$$C_t(z,t)=DC_{zz}(z,t) \tag{6}$$

a general solution for the evolving concentration distribution in the form [12]

$$C(z,t)=a_0+\sum_{n=1}^{\infty} a_n \cos\left(\frac{n\pi z}{L_1}\right)\exp\left[-\left(\frac{n\pi}{L_1}\right)^2 Dt\right], \tag{7}$$

with the Fourier coefficients

$$a_0=\frac{1}{L_1}\int_0^{L_1} g(z)dz \tag{8}$$

and

$$a_n=\frac{2}{L_1}\int_0^{L_1} g(z)\cos\left(\frac{n\pi z}{L_1}\right)dz. \tag{9}$$

Thus, after time t_1 at T_1 with diffusivity D_1,

$$C_1(z,t_1)=\frac{C_0 l_i}{L_1}+\sum_{n=1}^{\infty}\frac{2C_0}{n\pi}\sin\left(\frac{n\pi l_i}{L_1}\right)\cos\left(\frac{n\pi z}{L_1}\right) \times\exp\left[-\left(\frac{n\pi}{L_1}\right)^2 D_1 t_1\right]. \tag{10}$$

Next we assume that during the transition from T_1 to a T_2, the diffusive redistribution is insignificant. In view of he high ratio of thermal to solutal diffusivity of the materials under consideration, this is readily achievable in practice with rapid temperature ramping. Furthermore, we ignore the diffusant redistribution *due to* the thermal expansion or contraction of the sample during the temperature change. With typical thermal expansion coefficients of liquids, this simplification introduces significant errors only for simulation temperature changes in excess of 200 °C. Based on these assumptions, the initial condition at T_2 is taken as

$$g_2(z)=C_1(z,t_1). \tag{11}$$

Thus, accounting for the new sample length L_2, Eqs. (7)–(9) yield for the evolution of the concentration distribution at T_2 [10]

$$C_2(z,t)=a_{02}+\sum_{m=1}^{\infty} a_{m2}\cos\left(\frac{m\pi z}{L_2}\right)\exp\left[-\left(\frac{m\pi}{L_2}\right)^2 D_2 t\right], \tag{12}$$

where

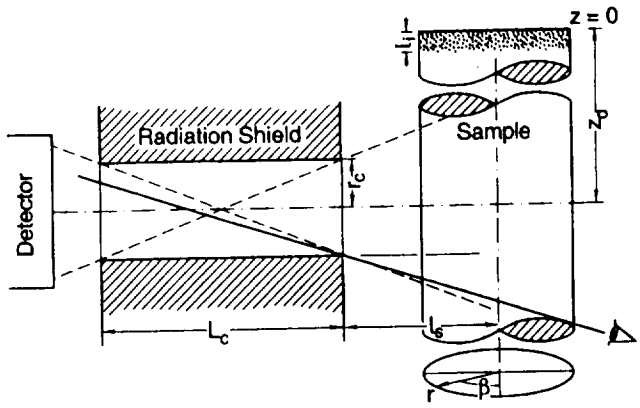

FIG. 3. Definition of sample-collimator-detector geometry for the view factor calculation.

$$a_{02}=\frac{C_0 l_i}{L_1}+\sum_{n=1}^{\infty}\frac{A_n}{L_2}\frac{L_1}{n\pi}\sin\left(\frac{n\pi L_2}{L_1}\right), \tag{13}$$

with

$$A_n=\frac{2C_0}{n\pi}\sin\left(\frac{n\pi l_i}{L_1}\right)\exp\left[-\left(\frac{n\pi}{L_1}\right)^2 D_1 t_1\right] \tag{14}$$

and

$$a_{m2}=\frac{2C_0 l_i}{m\pi L_1}\sin(m\pi)+\sum_{n=1}^{\infty}\frac{A_n}{\pi L_2}\left[\frac{\sin\left[\left(\frac{n}{L_1}-\frac{m}{L_2}\right)\pi L_2\right]}{\frac{n}{L_1}-\frac{m}{L_2}} + \frac{\sin\left[\left(\frac{n}{L_1}+\frac{m}{L_2}\right)\pi L_2\right]}{\frac{n}{L_1}+\frac{m}{L_2}}\right]. \tag{15}$$

Based on this formulation, we have simulated the evolution of the concentration distribution during entire experiment scenarios, including the multistep ramps to the first and consecutive measurement tempeatures [10].

B. View factor, absorption of radiation, and detector noise

For realistic estimates of the radiation received at the detector, the volume of sample visible through the collimation hole must be known. Hence we have calculated the view factor of the sample-collimator-detector geometry [10]. Assuming perfect absorption by the shield material, radiation escapes only through the collimation bore of diameter $2r_c$ and length L_c; see Fig. 3. Under this assumption, the number of emitters "seen" by the detector is

$$N(z_d)=\int_{-\pi/2}^{\pi/2}\int_0^{r_c}\int_{z_d-z_0}^{z_d+z_0}\frac{r_c^2\left\{2\cos^{-1}\left(\frac{h}{r_c}\right)-\sin\left[2\cos^{-1}\left(\frac{h}{r_c}\right)\right]\right\}rC(z)}{2\pi r_t^2}dz\,dr\,d\beta, \tag{16}$$

where

$$h=\frac{L_c}{2(l_s+r\sin\beta)}\left(\sqrt{r^2\cos^2\beta+z_0^2}-r_c\right)\times\theta\left(\sqrt{r^2\cos^2\beta+z_0^2}-r_c\right), \quad (17)$$

$$z_0=\sqrt{\left(\frac{r_c}{L_c}\left[L_c+2(l_s+r\sin\beta)\right]\right)^2-r^2\cos^2\beta}, \quad (18)$$

$r_l=(L_c+l_s)$ and $C(z)$ at the time of measurement is given by an equation similar to Eq. (12). As defined in Fig. 3, r,β,z are the coordinates within the sample, with $z=0$ at the end containing the radiation source of initial thickness l_i. The angle $\beta=-\pi/2$ is taken in the direction of the detector on the collimator axis.

In the actual simulation runs, we have included the attenuation of the radiation by both the emitter-location-dependent self-absorption (see Fig. 2) and the thermal radiation shields (see Fig. 6). Furthermore, the noise in the detectors, i.e., the uncertainty in the detector signals due to radiation counting statistics, was accounted for. This noise is of the order of $\sqrt{n}$, where n is the number of counts received. Thus the statistical uncertainty increases with counts, but the relative uncertainty decreases as $1/\sqrt{n}$ [9]. Hence the higher the count rate, the more accurate the results. This can be accomplished by either using a long counting period or high initial activity.

C. Sample dimensions and activity

The lengths of the activated section l_i and the overall sample L were optimized based on the following considerations. The above square-root dependence of the detector noise on sample activity suggests the use of high activities to maximize the resolution in the difference of the two detector signals. This in turn minimizes the measurement time required at a given temperature and thus the errors from continuous diffusion during a data acquisition period. Similarly, the initial activity required to ensure a given detector signal increases with sample length. However, low activity levels are desirable for radiation safety reasons. Simulation results (see Sec. III E) showed that an initial activity of 5 mCi provides sufficient resolution. With this initial activity, the optimum sample length is 30 mm [10].

To determine the length of the activated section l_i we recall our assumption that the part of the concentration profile viewed by a detector is linear; see Eq. (3). Thus the initially activated section must be short enough that the transient in which the spreading concentration distribution possesses significant curvature is over when the signal level at the second detector is high enough to begin measurements. The simulations yielded $l_i=1$ mm as optimum. Thus our diffusion samples consist initially of two parts: the 1-mm-long radioactive section and a 29-mm-long non-activated section.

D. Determination of collimator geometry

Geometric factors as well as radiation properties of the shielding material must be considered in optimizing the collimator geometry. Obviously, the radiation shield must be thick enough to absorb a large fraction of the radiation. Otherwise the detector signal is not representative of the radiation escaping through the collimation bores. Furthermore, as can be seen from Fig. 3, due to the conical shape of the radiation beam transmitted by the collimation bore, r_c's larger than the sample diameter will not result in a commensurate increase of the radiation dose received by the detector. These arguments are further complicated by the scattering of and fluorescence induced by the primary radiation [9]. Our samples (^{114m}In) emit about 95% γ and 5% β radiation, with the average β energy in excess of 750 keV. Both cause fluorescence in the shield. In addition, γ radiation is Compton scattered in the shield and, in particular, upon grazing incidence on the collimator surface. Each scattering process reduces the energy of the radiation. Thus multiple scattering and fluorescence can lead to photons that are counted in energy windows different from those corresponding to the primary photons and β particles.

We have experimentally investigated various collimator geometries for their effect on total radiation received by the detector. Hence we used lead for the collimator optimization experiments that were conducted at room temperature. Collimation holes of 1, 1.5, 2, and 3 mm diameter were drilled into lead shields of 12.7, 25.5, and 38.3 mm thickness. A 3-mm-diam cylindrical radioactive indium sample was placed consecutively behind the collimation bores. The detector signals were energy discriminated; see Sec. IV C. Table I summarizes the results. The signal-to-noise ratio is defined as the signal amplitude obtained in the energy window (± 0.3 keV about the chosen energy) divided by the sum of amplitudes measured in all other channels outside the energy window.

From these data, we can draw the following conclusions. Since the signal-to-noise ratio (SNR) for the 1-mm collimator hole is essentially 1, the smallest usable diameter is 1.5 mm. As expected, with the 3-mm sample diameter very little additional radiation is received on expanding the collimator diameter to more than 2 mm and, hence, the SNR remains essentially unchanged or even decreases. Furthermore, the signal-to-noise ratio increases with the increase in the thickness of the radiation shield, from 12.7 mm to 25.5 mm, while a 38.3 mm thickness results in little further improvement.

Copper, initially planned as the high-temperature radiation shield material, showed intolerably high fluorescence levels. For the actual high-temperature experiments, the radiation shield consisted of gold with a wall thickness of 15.5 mm. As calculated from absorption data [9], this wall thickness provides the same absorption for 190-keV photons as the 25.5 mm of lead used above. This results in an overall diameter of the radiation shield/isothermal liner of 41 mm. With this collimator geometry and 10-mm square detectors, the maximum distance between the outside edge of the collimator and detector must not exceed 30 mm if all radiation from the collimators is to be collected.

E. Simulated multitemperature experiments

Based on the above considerations, utilizing Eqs. (1)–(18) evaluated for the optimized dimensions of our experimental hardware, simulations were carried out to explore the feasibility and accuracy of measurements at several temperatures with the same sample. Table II shows for self-diffusion in indium that a temperature range of 700 °C can be covered in

TABLE I. Signal-to-noise ratios obtained with various collimator geometries.

Diameter (mm)	Lead thickness (mm)	Signal to noise ratio at 24 keV	Signal to noise ratio at 190 keV
1	12.7	1.1	1.1
1.5	12.7	1.4	1.25
2	12.7	1.67	1.5
3	12.7	2.1	2.0
1	25.5	1	1
1.5	25.5	1.6	1.6
2	25.5	2.0	1.8
3	25.5	2.0	2.1
1	38.3	1	1
1.5	38.3	1.9	1.5
2	38.3	2.2	1.9
3	38.3	1.7	2.2

100 °C increments using only two samples. The second column lists the input diffusivities [13] used in the simulations. The table illustrates well the importance of taking the detector noise into account. Without superposition of noise on the signals $n_1(t)$ and $n_2(t)$, the simulations unrealistically yield an error in all eight deduced diffusivity values of less than 0.2%; see the third and fourth columns. However, as shown by columns six and seven, on superposition of a realistic $\pm(O)2\sqrt{n}$ noise level, the errors increase to (a still very acceptable) 1.5%.

Note that it is advantageous to begin with the highest temperature and, thus, highest diffusivity in a measurement series and then to take data at consecutively lower temperatures. Obviously, at the highest diffusivity the time required until the signal at the second detector rises above background is minimized; see Eqs. (7)–(9). In addition, the simulations unexpectedly revealed another advantage of decreasing temperature sequences, in which the measurement time at each temperature is shorter than at the immediately following one. While at all temperatures the spreading of the concentration profile depends on the product of the respective D and measurement time [see Eqs. (7) and (12)], beginning with the second temperature there is an additional time-dependent spreading term [see Eq. (14)]. As a consequence, longer measurement times at the prior temperature, as they would be required in a sequence with increasing temperatures, cause a larger decrease in the overall concentration gradient. The simulations show that the resulting smaller differences between the two signals lead to fewer feasible temperatures in an experiment.

The above simulations provided valuable guidance for experiment design. However, they do not account for some of the error sources present in actual experiments. These include imperfect shielding and secondary scatter by the radiation shield and collimation bores. In Sec. IV D we will present procedures to at least partly correct for these errors using signals from background detectors. There are also significant systematic errors associated with the dimensional tolerances of the sample and collimator-detector geometry. These error sources are evaluated in Sec. IV E.

IV. EXPERIMENT

A. Sample preparation and containment

The sample consists of two parts: a short radioactive section and a long nonactivated section. The preparation and containment of these sections is based on the following considerations. Uncertainties in the sample geometry are the major error source in these experiments. Furthermore, the sample cross section must be uniform to assure one-

TABLE II. Comparison of simulation model input diffusivities and simulation results for two model runs at eight different temperatures.

Temperature (°C)	Input	Result without noise		Result with noise	
	10^5D (cm^2/sec)	10^5D (cm^2/sec)	% error	10^5D (cm^2/sec)	% error range
900	10.2226	10.2002	0.22	10.2589	<0.5
700	8.260 01	8.255 02	0.060	8.185 63	<1
500	5.978 81	5.978 31	0.0084	5.956 64	<1
300	3.456 23	3.456 21	0.000 72	3.498 95	<1.5
800	9.280 63	9.25 65	0.26	9.331 37	<0.5
600	7.158 44	7.154 24	0.059	7.100 53	<1
400	4.734 12	4.733 54	0.012	4.723 77	<1
200	2.210 22	2.2102	0.000 83	2.210 52	<1.5

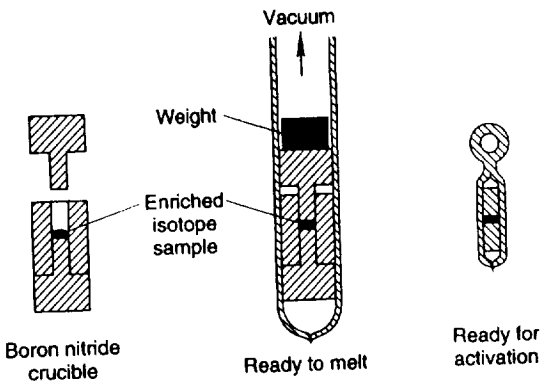

FIG. 4. Steps for preparation of the enriched isotope pellet for activation.

dimensional diffusion. Nonuniformities in the cross section can arise from capillarity (rounded edges at ends of both sections) and voids or bubbles in the sample bulk and at the interface between the two sample sections. Equally important is the accuracy in sample length and volume; see Sec. IV E. In addition, oxidation, in particular of the contacting ends of the sections, can form a diffusion-resistant layer. Hence, both the indium and boron nitride (BN) (Carborundum grade AXO5) container parts (BN is not wet by indium) are thoroughly high-vacuum baked (10^{-6} mm of Hg at 900 °C) to remove gaseous contaminants.

The radioactive section is prepared, as shown in Fig. 4, using a boron nitride crucible consisting of three parts machined with tight tolerances. After insertion of the bottom plug into the 3-mm-i.d. cylinder, a bead of indium (40% enriched in ^{113}In) is put in place. The weight of the bead is chosen such that the thickness of the final disk will be approximately 1 mm. After insertion of the top plug, the whole crucible, with a small weight on the top, is inserted into a glass tube. This is followed by vacuum heating to 900 °C and solidification of the sample under high vacuum while it is compressed by the weight. After cooling, we backfill with argon. Then the section is prepared for irradiation. Utilizing a glove box, the glass tube is broken and the sample is transferred to a 3-mm-diam glass capillary. To facilitate sample removal after irradiation, 5-mm-long rods are placed above and below the sample prior to sealing of the capillary. The sealed-in section is then sent to the reactor for activation by fast neutron irradiation.

The 29-mm-long nonactivated section of the sample is cast in place under high vacuum at 900 °C in the boron nitride ampoule used for the diffusion measurements. As depicted in Fig. 5, this 7-mm-o.d. ampoule is 60 mm long and has a 3-mm precision-reamed bore. To ensure the proper sample length we require square corners on the top and bottom ends of the sample. At the bottom this is achieved by press fitting a BN plug into the ampoule bore. At the top we apply a slight pressure on the sample with a weak graphite spring [Energy Science Laboratories, force 29.4 mN (3 g) at 900 °C] against a BN plunger that has less than 0.025-mm clearance in the bore. To establish conditions that ensure the absence of void formation, inactive sections were repeatedly melted, solidified, and x-ray inspected.

Then the activated section is transferred into the ampoule in a glove box flushed with an inert gas. After replacing the plunger and spring, the BN ampoule is mechanically closed with the BN screw lid and inserted into the square-bottom silica tube, which, in turn, is evacuated and sealed.

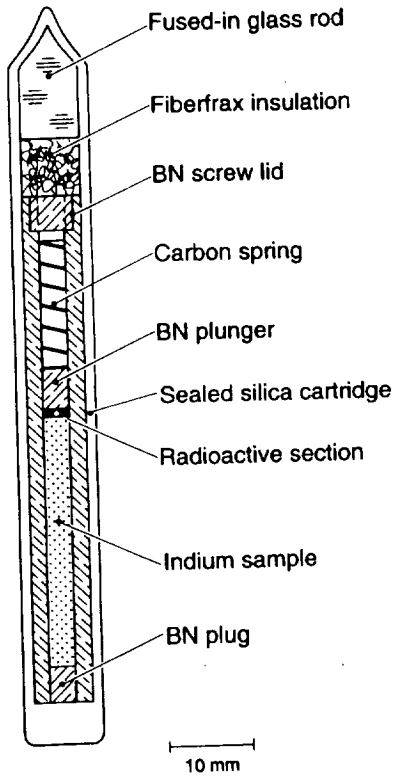

FIG. 5. Cross section of diffusion sample cartridge.

B. Diffusion measurement apparatus

The apparatus, which accommodates the above sealed diffusion sample cartridge, consists of the following components (see also Fig. 6). There is a gold radiation shield and isothermal liner (90 mm long, 41 mm in diameter). Gold was chosen because of its high melting point and thermal conductivity together with the low fluorescence and high radiation absorption properties. To minimize displacement of this gold cell by thermal expansion it is supported by a silica pedestal (thermal expansion coefficient 5.5×10^{-7} cm/cm °C). There is a stainless-steel-encased, ceramically insulated resistance heater (Fast Heat, 130 mm long, 120 V, 5 A). To avoid radiation absorption, the heater has six holes (7 mm in diameter) at the positions of the collimators and background detectors. Thermocouples (type *K*) are inserted into the gold liner for temperature uniformity control. One of these provides input to a temperature controller and silicon controlled rectifier that stabilizes the temperature to better than ±0.5 °C. An inner thermal radiation shield consists of a stainless-steel sheet. An outer thermal shield consists of gold-coated boro-silicate glass. There are six radiation detectors (not shown): one pair each aligned with the oppositely placed, differently spaced radiation bores (see Sec. II B) and one pair 90° off the measurement-detector plane to record the background radiation. Top and base plates contain the measurement structure. Axial heat losses from the heated components to these plates are minimized by Fiberfrax insulation.

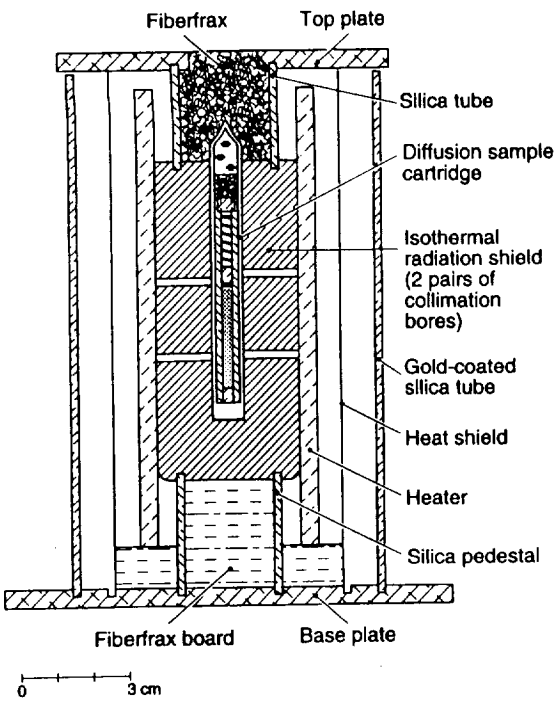

FIG. 6. Cross section of diffusion measurement apparatus (without detectors and electronics). Note the two pairs of collimation bores, offset with respect to each other, to cover the temperature range 300 °C–900 °C for indium.

The temperature uniformity across the diffusion sample in this apparatus was checked using a dummy diffusion sample cartridge with eight built-in, calibrated thermocouples (type K, sheath diameter 0.5 mm, Omega Engrg.). At 500 °C, the vertical temperature difference ΔT_v across the indium sample (see Fig. 5) was 0.4 °C, with the bottom cooler than the top. At the same time the maximum horizontal ΔT_h, which occurred at about midheight of the sample, was 0.3 °C. At 900 °C, we obtained a $\Delta T_v = 1.4$ °C of the same orientation and a maximum $\Delta T_h = 0.4$ °C at the top of the sample.

An important design consideration for the use of the apparatus over a wide temperature range is the thermal expansion of the components, which changes the spacing of the collimation bores and their position with respect to the detectors. The changes in the bore spacing, which over a temperature range of 700 °C is about 0.4 mm, is taken into account when applying Eq. (3). The changing bore locations with respect to the fixed detector positions are taken into account by using detector crystals large enough that the emanating radiation cone remains fully detected during the thermal displacement.

C. Detectors, discriminators, and calibration

After examining numerous detector types, we have found that $Cd_xZn_{1-x}Te$ crystals (eV Products, 1 cm^2 and 3 mm thick) provide a quantum efficiency of approximately 1 for the 24-keV photons and 0.35 for the 190-keV photons of indium. In addition, these detectors exhibit a low noise threshold ($\leq$10 keV) at temperatures $\leq$50 °C, i.e., no additional cooling is required. Two single-channel analyzers (SCAs) per detector can be set using four potentiometers on the circuit boards providing a 0–250 keV energy range.

Due to differences in the characteristics of individual crystals and detector circuits each detector must be independently calibrated. The calibration is accomplished using a multiple-channel analyzer (MCA) (Accuspec, NaI, Canberra Instruments) and a data acquisition system with a counter for each energy channel. The calibration of each detector SCA energy window is performed by matching the SCA output count rate and the chosen MCA energy window count rate.

D. Measurement procedure

After loading the sealed sample ampoule into the gold cell and repacking the thermal insulation, the temperature is ramped at 15 °C/min to the highest experiment temperature. After the signal at the $5L/6$ detectors has sufficiently risen above background, data acquisition begins. The measurement times at this first and consecutive, lower temperatures are predetermined based on the simulation results. After diffusant uniformity has been obtained throughout the sample, we return to each experiment temperature and collect baseline averages. These data are used to correct for inconsistencies of the detector crystals and possible abnormalities in the collimator-detector geometry. One detector-channel is selected as being "correct" and, using the averages at each temperature, all other channels are proportionally adjusted. The same is done with the two background detectors. The background is subtracted from all channels and then Eq. (3) is applied to find the concentration at all times.

With sources activated to 5–10 mCi we can typically obtain data at three separate temperatures per run. The simulations suggested the feasibility of four temperatures. However, in the simulation we did not allow for cool down periods between temperatures. At lower temperatures these periods can be up to an hour for a 200 °C change.

E. Estimation of uncertainty in apparent diffusivity

As expressed in Eq. (2), the diffusivity D is obtained from the slope of a straight line fit to $\ln[n_1(t)-n_2(t)]$. We have shown earlier that such straight line plots can be obtained even in diffusion experiments with considerable convective contamination [14]. Hence, considering the deviations from isothermality of our samples (see Sec. IV B) and thus likely resulting convective transport, the following estimate of uncertainty in D must be understood with respect to the apparent rather than the true diffusivity. This uncertainty can be expressed in terms of the uncertainties in the slope and the sample length as [15]

$$\delta D = \sqrt{\left[\left(\frac{L}{\pi}\right)^2 \sigma_B\right]^2 + \left(\frac{2LB}{2}\,\delta L\right)^2}, \tag{19}$$

where the slope $B = -\pi^2 D/L^2$ and $\sigma_B^2 = N\sigma_y^2/\Delta$, with N the number of data points used in the fit, and $\Delta = N(\Sigma_{i=1}^N t_i^2) - (\Sigma_{i=1}^N t_i)^2$ and $\sigma_y^2 = [1/(N-2)]\Sigma_{i=1}^N (y_i - A - Bt_i)^2$, with $y = \ln(n_2 - n_1)$ and A (the y intercept) = const.

The uncertainty in the length of the sample can be estimated as follows. The sample is made of two sections (see Sec. III C) producing an uncertainty

TABLE III. Apparent self-diffusivities obtained with indium at the two photon energies in four experiments.

Temperature (°C)	190 keV ($10^5 D$ cm^2/sec)	24 keV ($10^5 D$ cm^2/sec)
800	9.84±0.59	10.07±0.61
600	7.69±0.48	8.02±0.50
400	5.25±0.34	5.01±0.34
700	7.72±0.47	
500	6.20±0.39	
300	4.60±0.33	
900	8.95±0.54	8.61±0.52
800	9.80±0.59	10.16±0.61
700	8.93±0.55	9.62±0.60
900	11.75±0.70	11.63±0.59
600	8.04±0.49	8.09±0.50
300	4.54±0.29	4.78±0.31

$$\delta L = \delta l_i + \delta l_{\mathrm{NA}}, \tag{20}$$

where l_{NA} is the length of nonactivated sample. The uncertainty in the two sections is determined from the volume and machining of the crucibles such that

$$\delta l = \sqrt{\left(\frac{1}{\pi r^2}\,\delta V\right)^2 + \left(\frac{2V}{\pi r^3}\,\delta r\right)^2}, \tag{21}$$

with r the radius of the crucible and V the volume of sample material. If we assume that the density ρ is accurately known, then the uncertainty in the volume is

$$\delta V = \left|\frac{1}{\rho}\right| \delta m. \tag{22}$$

The tolerance on the crucibles is ±0.0127 mm (nominal sample inner diameter 3.01 mm). Due to the repeated vacuum melting, the uncertainty in the masses is 0.001 g.

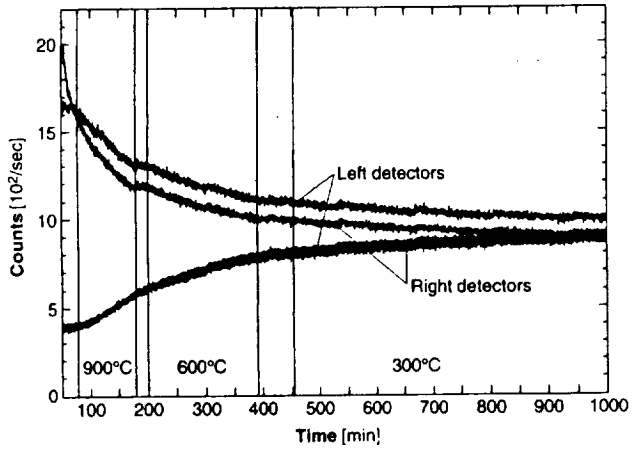

FIG. 7. Original signal traces for 190-keV photons during the 900 °C–300 °C run.

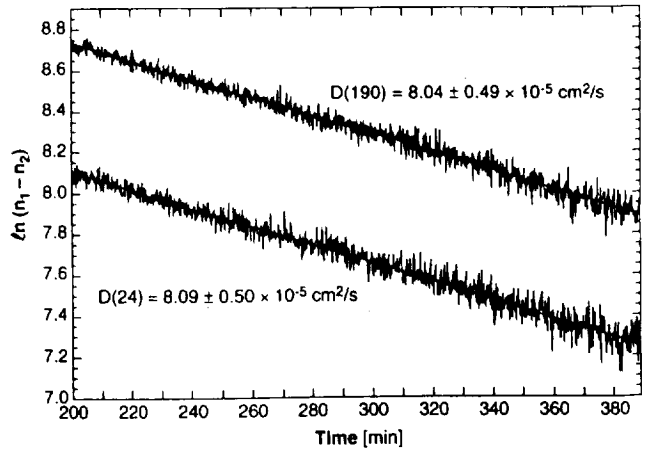

FIG. 8. Plot of 600 °C data of 900 °C–300 °C according to Eq. (2), together with diffusivities obtained from least-squares fits (straight lines).

Substituting Eq. (22) into Eq. (21) and the result into Eq. (20), the uncertainty in the length of the sample is ±1.02 mm for indium.

The σ_B error is directly related to the counting statistics. This error is minimized with high initial activities. With the activity levels chosen for these experiments we find that the second term in Eq. (19) is up to an order of magnitude larger than the first.

V. RESULTS AND DISCUSSION

Several diffusion runs with indium were carried out. Each run covered three consecutively lower temperatures. The results are summarized in Table III. The error estimates are based on Eq. (19). The lack of 24-keV data for the one run is due to failure of one low-energy channel. Note that, within the uncertainty of the data, no difference between transport (diffusion) in the bulk and near the wall is apparent.

As-measured time traces of the 190-keV signals obtained in the 900 °C–300 °C run (Table III) are shown in Fig. 7. These plots reveal several features of the method. The right top detector has the highest initial count rate since its position $z_1 = L/6$ has been chosen for the highest $T = 900$ °C, i.e., the longest L; see Sec. II B. The change in the diffusion coefficient at the three temperatures is visible in the slope changes of the data. Furthermore, the contraction of the sample on temperature decrease is evident from the rise in the count rate. One sees also that the final count rates of the detectors differ, due to the individual characteristics of the detector crystals; see Sec. IV D. A plot of $\ln(n_1 - n_2)$ vs time, resulting from similar curves obtained at 600 °C after their base-line corrections, is shown in Fig. 8 together with the least-squares fits for both energies.

All data from Table III together with the self-diffusivities of In measured by other authors [4,13,16,17,18], are plotted in Fig. 9. The wide scatter of the data illustrates well that diffusivities obtained in liquids at normal gravity are prone to be contaminated by uncontrollable convection. As emphasized for liquid diffusivity measurements by Verhoeven [19], any horizontal component of a density gradient results in convection without a threshold. We have recently estimated

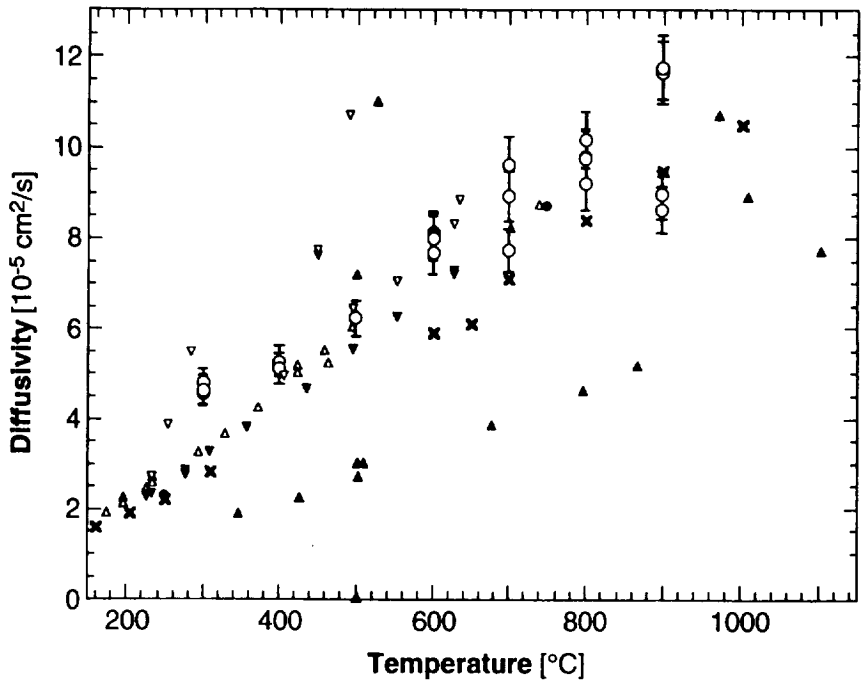

FIG. 9. Experimental data for self-diffusivities in indium: ○ this work; ▲ Foster and Reynik [17]; △ Lodding [13]; ● Mathiak *et al.* [16]; ▽ and ▼ Carreri, Paoletti, and Vincentini [4] with 1.6- and 0.83-mm-diam capillaries, respectively. Ogloblya, Lozovoi, and Chumakov [18] with 0.5-mm-diam capillaries.

convective contributions to transport in our experiments [14]. The numerical modeling results for self-diffusion in In at 730 °C in 30-mm-long capillaries, 3 mm in diameter, show that at normal gravity convective contributions become significant when an applied horizontal temperature non-uniformity ΔT_h exceeds 0.01 K. Often, flow due to horizontal density gradients can be reduced by keeping, as is the case in our experiments (see Sec. IV B) the top of the sample slightly warmer than its bottom. However, the above simulations [14] show that this can be rather ineffective and under certain conditions may even increase the apparent diffusivity.

From the above, it is not surprising that our data show evidence of convection in the samples. For instance, the apparent D at 700 °C deduced from the 900 °C–700 °C run is significantly higher than that of the 700 °C–300 °C run. This may be due to the longer time the first sample was at high temperature before the measurement at 700 °C was made. Thus there was more time for convective contamination of the diffusive transport. Note, however, that the uncertainties for the two measurements at 900 °C do not overlap. We assign this to possible inconsistencies in the sample preparation and convective contributions. The low value may be the result of partial blockage of the diffusion path by either a void or an oxidation layer between the active and inactive sections of the sample.

IV. SUMMARY AND CONCLUSIONS

We have developed and systematically optimized a technique for the *in situ* measurement of diffusivities in liquids at several temperatures with one sample. This approach circumvents the solidification of the diffusion sample required by other methods, which can result in significant errors. In experiments with ^{114m}In/In, apparent self-diffusivities were obtained between 300 °C and 900 °C with an uncertainty of ±5%. By utilizing the different self-absorption characteristics of the 24- and 190-keV photons of ^{114m}In, transport in the bulk of the sample and near the container wall was investigated independently. No differences were found. There is clear evidence for convective contamination of our data. To obtain increased accuracy in the diffusivity values, we plan to perform these experiments in a low-gravity environment.

ACKNOWLEDGMENTS

We thank W. F. Kaukler from our center for help with the x-ray inspection of diffusion samples. L. Carver has expertly prepared the figures. Support for this work by the Microgravity Science and Applications Division of the National Aeronautics and Space Administration through Contract No. NAS8-39716 is gratefully acknowledged.

[1] M. Shimoji and T. Itami, *Atomic Transport in Liquid Metals* (Trans Tech, Aedermansdorf, 1986).

[2] N. H. Nachtrieb, Ber. Bunsenges. **80**, 678 (1976).

[3] N. H. Nachtrieb, in *Proceedings of the International Conference on Properties in Liquid Metals*, edited by P. D. Adams, H. A. Davies, and S. G. Epstein (Taylor and Francis, London, 1967), p. 309.

[4] G. Careri, A. Paoletti, and M. Vincentini, Nuovo Cimento **10**, 1088 (1958).

[5] M. Fixman, J. Chem. Phys. **29**, 540 (1958).

[6] S. B. Savage and R. Dai, Mech. Mater. **16**, 225 (1993).
[7] G. Mo and F. Rosenberger, Phys. Rev. A **44**, 4978 (1991).
[8] P. Codastefano, A. Di Russo, and V. Zanza, Rev. Sci. Instrum. **48**, 1650 (1977).
[9] W. H. Tait, *Radiation Detection* (Butterworths, London 1980).
[10] L. Jalbert, Ph.D. dissertation, University of Alabama, Huntsville, 1997 (unpublished).
[11] N. Tsoulfanidis, *Measurement and Detection of Radiation* (McGraw-Hill, Washington, DC, 1983).
[12] J. Crank, *The Mathematics of Diffusion* (Clarendon, Oxford, 1956).
[13] V. A. Lodding, Z. Naturforsch. **11A**, 200 (1956).
[14] I. Alexander, J.-F. Ramus, and F. Rosenberger, Microgravity Sci. Technol. **9**, 158 (1996).
[15] J. R. Taylor, *An Introduction to Error Analysis* (University Science Books, Oxford, 1982).
[16] G. Mathiak *et al.*, J. Non-Cryst. Solids **205-207**, 412 (1996).
[17] J. P. Foster and R. J. Reynik, Metall. Trans. A **4**, 207 (1973).
[18] V. I. Ogloblya, V. I. Lozovoi, and A. G. Chumakov, Phys. Metals **9**, 455 (1990).
[19] J. D. Verhoeven, Trans. Metall. Soc. AIME **242**, 1937 (1968).

J. Phys.: Condens. Matter 10 (1998) 7113–7120. Printed in the UK PII: S0953-8984(98)93529-9

On the insensitivity of liquid diffusivity measurements to deviations from 1D transport

Lyle B Jalbert, Franz Rosenberger and R Michael Banish

Center for Microgravity and Materials Research, University of Alabama in Huntsville, Huntsville, Al 35899, USA

Received 22 April 1998

Abstract. In liquid diffusion experiments, the diffusion path can be partially obstructed by bubbles/voids, or oxide layers between the segments of a diffusion couple. In addition, there have been claims of macroscopic manifestations of 'wall effects', i.e. a perceived dependence of the diffusivity D on distance from the container wall over macroscopic dimensions. We have numerically simulated the evolution of the concentration field in a 2D diffusion sample in response to such deviations from 1D transport. We found that, owing to the smoothing of the concentration distribution by radial diffusion, significant deviations from the ideal 1D concentration field occur only in the axial direction. On evaluation of the concentration field for an apparent diffusivity D_a, either by the semi-infinite capillary methodology or by the method of Codastefano *et al* (1977 *Rev. Sci. Instrum.* **48** 1650), we found that local obstructions of the transport path have to be in excess of half the transport path's cross-section to result in $D_a \leqslant 0.95D$. Furthermore, we conclude that the radial concentration gradients found in solidified diffusion samples are no evidence for a 'wall effect' but are likely to indicate convective transport contamination.

1. Introduction

Bubbles or voids in liquid diffusion samples [1,2] can potentially result in erroneous diffusivity determinations. It may also be difficult to prevent the formation of oxide layers, which represent a barrier in the diffusion path, between the segments of a metallic diffusion couple. Other perturbing phenomena observed in diffusion measurements have been generically assigned to 'wall effects' [3–5]. By analogy with surface and grain boundary diffusion, it is speculated that the diffusivity D varies over macroscopic dimensions from the container wall. However, as pointed out by Nachtrieb [5], irrespective of the possible underlying mechanism, 'It is, of course, not credible that a true wall effect could extend much further than a few atomic diameters from the capillary wall, and a reasonable explanation in terms of an experimental artifact must be sought.'

In the following we will examine to what extent such deviations from 1D transport, whether real or conceived, influence the evolution of the concentration distribution in a diffusion sample. In addition we will evaluate the resulting non-ideal distributions in terms of apparent diffusivities D_a utilizing both the semi-infinite sample methodology [6] and the method of Codastefano *et al* [7].

In the semi-infinite technique [6], the diffusion sample is assumed to be infinite in one direction, i.e. with a diffusion path of length L, the initial thickness h of the diffusant source

0953-8984/98/327113+08$19.50

(with uniform concentration C_0) must fulfil the condition $h \ll L$. This condition results in the concentration profile at time t

$$C(x,t) = \frac{C_0}{\sqrt{\pi Dt}} \exp\left(\frac{-x^2}{4Dt}\right). \tag{1}$$

Thus, a plot of $\ln C$ against x^2 produces a straight line with the slope given by $-1/(4Dt)$.

In the Codastefano technique [7], one monitors the solute concentrations against time at the positions $x = L/6$ and $5L/6$. The resulting time traces $C_1(t)$ and $C_2(t)$, respectively, are related to the diffusivity through a straight line fit in the form

$$\ln[C_1(t) - C_2(t)] = \text{constant} - \left(\frac{\pi^2 D}{L^2}\right) t. \tag{2}$$

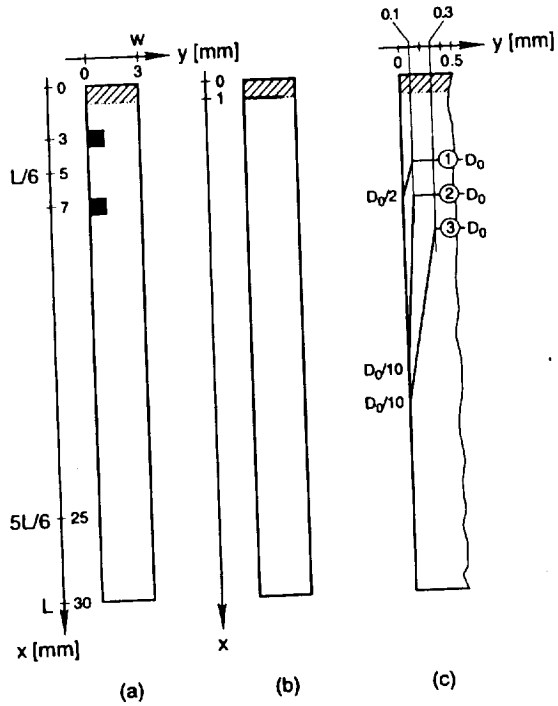

Figure 1. Geometry and modifications of simulation model. Diffusion capillary with (a) voids in liquid, (b) barrier at the source–solvent interface, and (c) y-dependent Ds. Shaded areas indicate regions of initial diffusant concentration C_0.

2. Simulation model

The basic geometry of the 2D simulation model and the various modifications used in the simulations are depicted in figure 1. In accordance with our experimental approach [8], we chose a total sample length $L = 30$, sample width $w = 3$ mm, and initial diffusant layer thickness $h = 1$ mm. Three different sets of conditions resulting in deviations from 1D diffusive transport were assumed. (a) A 1 mm square barrier on one wall, to simulate a void, was centred at $x = 3$ or $x = 7$ mm. Note that these particular positions straddle the Codastefano measurement coordinate $L/6$ at $x = 5$ mm (figure 1(a)). (b) A planar barrier

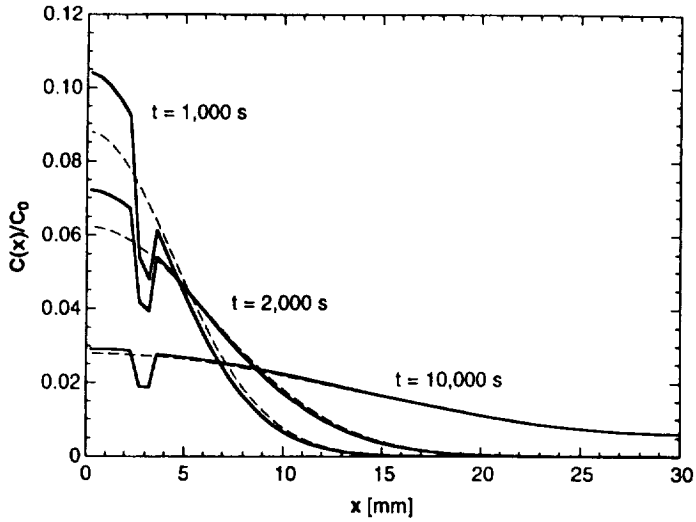

Figure 2. Normalized concentration profiles at three diffusion times. Full curves, with void at $x = 3$ mm; broken curves, unobstructed diffusion.

in the source–solvent interface was extended from one wall to either $y = 0.5$ or $0.75w$ (figure 1(b)). (c) A y-dependent diffusivity was assumed, with either $D = 0.5$ of the input diffusivity D_0 at the wall and then a linear rise to D_0 at $y = 100$ μm, or $D = 10^{-1}D_0$ at the wall rising to D_0 at either 100 or 300 μm; see the schematic D-profiles 1–3 in figure 1(c). The value of 100 μm represents the range at which a change attributed to the 'wall effect' was determined in [6]. The distance $y = 300$ μm corresponds to the sample depth from which 24 keV photons are received in our self-diffusivity measurements with indium [8].

Since isothermal self-diffusion was assumed, the fluid density is uniform throughout the diffusion process. Hence, solutions of the 2D diffusion equation

$$\frac{\partial C}{\partial t} = \frac{\partial}{\partial x_i}\left(D\frac{\partial C}{\partial x_i}\right) \tag{3}$$

where C is the solute mass concentration and $i = 1, 2$, fully describe transport in this case. We used $D_0 = 10.22 \times 10^{-5}$ cm^2 s^{-1} in all our numerical simulations, which corresponds to the self-diffusivity of indium at 900 °C [9].

The numerical simulations were performed with Adaptive Research's CFD 2000 finite volume code, version 3.03. In the void and barrier cases a non-uniform grid of 62×30 and 61×40, respectively, was used. For the wall investigations only half the cell ($0 \leqslant y \leqslant 1.5$ mm) was modelled, utilizing a 100×61 grid. Doubling of the grid number in the x- and y-direction in both the $y = 3$ mm void and 75% barrier cases (the cases with largest concentration gradients) resulted in insignificant changes in the concentration field. All cases were run for 10 000 s to obtain sufficient diffusant concentrations at the $5L/6$ position. For comparison with pure 1D diffusion an unobstructed, uniform-diffusivity run was performed with each grid.

Diffusivities are typically deduced from the total amount of diffusant contained in cross-sectional slices of the sample. Correspondingly, we base our evaluations of the apparent diffusivity D_a in the various cases on axial profiles of the concentration summed across y,

i.e. on

$$C(x,t) = \sum_{y=0}^{w} C(x,y,t). \tag{4}$$

Evaluations using the semi-infinite sample methodology were based on the $C(x,t)$-profile obtained at $t = 2000$ s, at which time the solute barely reaches L. The Codastefano *et al* methodology was applied to the $C(L/6,t)$ and $C(5L/6,t)$ traces obtained, depending on the case, between 3000–5000 and 10 000 s with samples taken every 10 s.

3. Results and discussion

Figure 2 shows $C(x)$-profiles obtained in the case with a void at $x = 3$ mm at three diffusion times. For comparison, we have also plotted the profiles resulting at these times in the 1D diffusion (void-free) case. Both sets of profiles were normalized with respect to C_0. We see that the presence of the void, which blocks one third of the sample cross-section, significantly retards the diffusive spreading of the solute. This is further illustrated by the isoconcentration lines in the upper end of the sample displayed for $t = 1000$ s in figure 3. Note that, as a result of radial diffusion the isoconcentration lines become essentially straight and normal to the x-axis within a short distance downstream from the transport-obstructing void.

Table 1. Apparent diffusivities (10^{-5} cm^2 s^{-1}) obtained in void configurations.

	1D transport	Void @ 3 mm	Void @ 7 mm
Semi-infinite method	10.44 ± 0.174	10.18 ± 0.72	10.17 ± 0.80
Codastefano method	10.2000 ± 0.0001	10.240 ± 0.001	9.9800 ± 0.0005

Table 1 displays the D_a-values obtained for the two void cases and the 1D results, together with respective standard deviations associated with the fits. Interestingly, the 1D transport run, evaluated with the semi-infinite approach, yielded a slightly elevated diffusivity compared with the input $D_0 = 10.22 \times 10^{-5}$ cm^2 s^{-1}. This is not surprizing since the initial source thickness, $h = 1$ mm, only poorly fulfills the required $h \ll L$ condition. Note that all void cases result in D_a-values that are within a few per cent of D_0. Hence, errors introduced by the presence of these voids remain below the experimental resolution, which is of order 5% [8, 10, 11].

Furthermore, table 1 shows that the location of the void has different effects on the apparent diffusivities calculated from the two methods. The semi-infinite sample technique is affected equally regardless of void location while the Codastefano method shows an increase/decrease in D_a with the void upstream/downstream of the $L/6$ measurement location. This, plus the drastically lower standard deviation of the second methodology indicated in tables 1–3, results from the different nature of the input data. The first fitting procedure utilized the $C(x)$-profile that (a) is locally strongly deformed by the void, and (b) is based on a finite resolution grid with 62 points. The Codastefano method, on the other hand, benefits from (a) the smooth variation of $C(x)$ at the two sampling locations ($L/6$ and $5L/6$, i.e. $x = 5$ and 25 in figure 2), and (b) the of O(500) data points used in the fit.

Figure 4 shows the axial profiles $C(x)/C_0$ obtained with the 75% barrier (figure 1(b)) at three diffusion times together with the corresponding profiles resulting on the same grid from the unobstructed 1D diffusion case. One sees that this barrier causes a pronounced

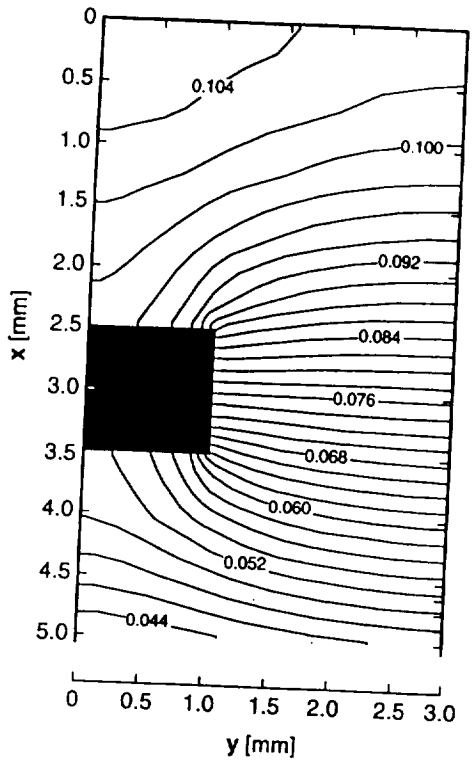

Figure 3. Normalized isoconcentration lines $C(x, y)/C_0$ in the upper part of the capillary at $t = 1000$ s with void at $x = 3$ mm.

Table 2. Apparent diffusivities (10^{-5} cm^2 s^{-1}) obtained in barrier configurations.

	1D transport	50% barrier	75% barrier
Semi-infinite method	10.45 ± 0.19	10.05 ± 0.42	9.59 ± 0.90
Codastefano method	10.2000 ± 0.0002	10.1600 ± 0.0004	10.050 ± 0.002

Table 3. Apparent diffusivities (10^{-5} cm^2 s^{-1}) obtained with 'wall effects'.

	1D transport	$D(y)$ case 1	$D(y)$ case 2	$D(y)$ case 3
Semi-infinite method	10.46 ± 0.19	10.29 ± 0.19	10.15 ± 0.19	9.55 ± 0.20
Codastefano method	10.1900 ± 0.0002	10.0400 ± 0.0002	9.9000 ± 0.0002	9.3000 ± 0.0003

retention of the solute in the region of initial diffusant location. However, table 2 reveals that even in this drastic case, the error in the deduced diffusivities is barely larger than the above typical experimental uncertainties. Here again the semi-infinite method is somewhat more sensitive than the Codastefano method.

The results of the various assumed 'wall effects' are summarized in table 3. Even with the particularly unphysical assumption of case 3, D_a-values are obtained that lie within the uncertainty of many measurements.

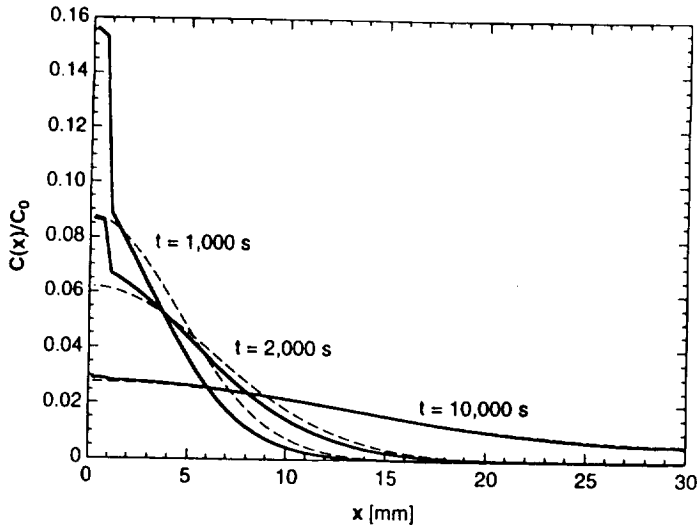

Figure 4. Normalized concentration profiles at three diffusion times. Full curves, with 75% barrier at $x = 1$ mm; broken curves, unobstructed diffusion.

Table 4. Maximum normalized radial concentration variation at $x = L/6$.

Case	Radial $\Delta C/C$ (%)	Time of occurrence (s)
$D(y)$ case 1	0.014	250
$D(y)$ case 2	0.028	230
$D(y)$ case 3	0.082	230

The insensitivity of the concentration distribution to postulated 'wall effects' is further illustrated in figure 5, in which we have plotted the concentration difference (normalized to the samples maximum C) between case 3 and the 1D transport result at 300 s. It is evident that solute redistribution by radial diffusion prevents the formation of significant concentration gradients across the width of the sample. This is also supported by the low values of the maximum radial concentration variation at position $x = L/6$ listed in table 4.

Note that these maxima occur early in the diffusion runs. Thus they are unlikely to be detectable in diffusivity measurements. As a consequence, experimental findings of radial concentration gradients in cylindrical diffusion samples indicate convective contamination (for detailed examples see [12]) rather than inferred dependences of diffusivity on the distance from the container wall.

4. Conclusions

The above 2D simulations show that the influence of the model voids, barriers and 'wall effects' on concentration distributions in diffusion samples and the subsequently deduced diffusivities is rather marginal. Note that in real, 3D systems, owing to the lower cross-sectional fraction taken on by such obstacles of the same radial dimensions, the deviations from unobstructed diffusive transport will be even less significant. Hence, we conclude that the contamination of diffusivity measurements owing to such geometrical parameters will in

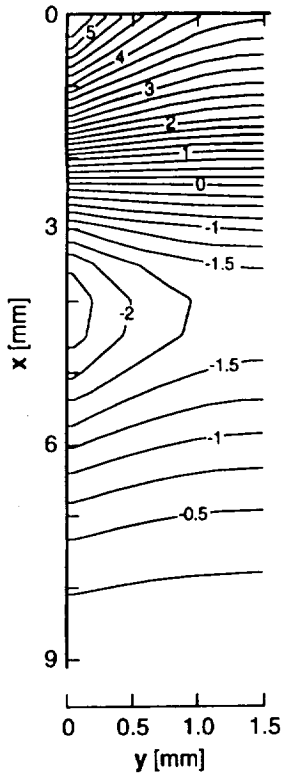

Figure 5. Difference in concentration between the 'wall effect' case 3 and uniform diffusion, $\Delta C(x, y)$, normalized to the maximum concentration, obtained in the top part of the sample at $t = 300$ s. Numbers in 10^{-2}%.

most cases be negligible compared with the convective contamination arising from sample non-isothermality [12].

Acknowledgments

This research has been supported by the National Aeronautics and Space Administration under contract NCC8-99, and by the State of Alabama through the Center for Microgravity and Materials Research at the University of Alabama in Huntsville. We are much obliged to J I D Alexander for advice on the use of the CFD code.

References

[1] Pollman K W, Stodieck L S and Luttges M W 1994 *Microgravity Sci. Tech.* **7** 50
[2] Weinberg F and Mui C 1994 *Can. Metal. Quart.* **33** 233
[3] Careri G, Paoletti A and Vincentini M 1958 *Nuovo Cimento* **10** 1088
[4] Foster J P and Reynik R J 1973 *Met. Trans.* **4** 207
[5] Nachtrieb N H 1967 *Proc. Int. Conf. on Properties in Liquid Metals* ed P D Adams, H A Davies and S G Epstein (London: Taylor and Francis) p 309
[6] Crank J 1956 *The Mathematics of Diffusion* (Oxford: Clarendon)
[7] Codastefano P, Di Russo A and Zanza V 1977 *Rev. Sci. Instrum.* **48** 1650

[8] Jalbert L B, Banish R M and Rosenberger F 1998 *Phys. Rev.* E **57** 1727
[9] Lodding V A 1956 *Z. Naturf.* a **11** 200
[10] Nachtrieb N H 1976 *Berichte Bunsenges.* **80** 678
[11] Simoji M and Itami T 1986 *Atomic Transport in Liquid Metals* (Aedermansdorf, Switzerland: Trans. Tech.)
[12] Alexander J I D, Ramus J-F and Rosenberger F 1996 *Microgravity Sci. Tech.* **9** 158

J. I. D. Alexander, J.-F. Ramus, and F. Rosenberger

Numerical Simulations of the Convective Contamination of Diffusivity Measurements in Liquids

Ideally, self-diffusivity measurements should be conducted under isothermal conditions. This is difficult to achieve in practice, particularly at high temperatures. Hence, we have assessed the effect of buoyancy-driven convection in liquid-filled vertical diffusion capillaries with slight azimuthal thermal asymmetries on their walls and ends. A tracer of same density as the liquid is initially located at one end of the capillary. Calculations of the 3D-time-dependent transport of the tracer, based on properties of liquid indium at 1,000 K, yielded a variety of results with practical implications. We found that with horizontal temperature nonuniformities across the sample as low as 1 and 0.1 K, respectively, convective transport in capillaries of 1 and 3 mm diameter can exceed diffusive transport. Superimposed vertically "stabilizing" temperature gradient did not sufficiently reduce these convective transport contributions. Hence, the widely used approach of keeping the top of the capillary slightly warmer than the bottom appears to be an ineffective means of "preventing convection". Most strikingly, we found that diffusive-convective transport can result in axial concentration profiles that are analytically indistinguishable from pure diffusion profiles. This casts considerable doubt on various graphical criteria previously used to demonstrate the absence of significant convective contamination in diffusivity data. Furthermore, these results reinforce the necessity of conducting diffusion measurements in liquids under microgravity conditions where convective contamination can be minimized or avoided entirely.

1 Introduction

Measurements of diffusion coefficients in liquids by macroscopic techniques are prone to be contaminated by convection. For example, in a system with a diffusivity of 10^{-5} cm^2/s and a diffusion distance of 1 cm, the characteristic diffusion velocity is of the order of 10^{-5} cm/s. Thus, if convective transport rates are not to exceed 1 % of the diffusive transport rates, convective flow velocities must not exceed 10^{-7} cm/s. In liquid self-diffusion experiments, buoyancy arises only due to density gradients introduced by temperature nonuniformities. Around room temperature, sufficient sample isothermality can be maintained to avoid significant convective flows. However, at the elevated temperatures characteristic of liquid metals and semiconductors, it is difficult to realize isothermal conditions to an extent that convection remains insignificant. This was recognized, in particular, by *Verhoeven*, who emphasized that any horizontal component of a density gradient results in spontaneous convection with no threshold [1]. Since then, in an attempt to reduce the flow from horizontal density gradients by applying a vertical, stabilizing one, it has become widespread practice to keep the top of diffusion capillaries slightly warmer than their bottom end.

Convection can be effectively reduced by reducing the characteristic distance for momentum transport in the (diffusing) liquid. However, a systematic experimental investigation has revealed convective contributions in vertical capillaries with diameters as small as 0.7 mm [2]. The same work has shown that concentration plots versus the square of the distance along the diffusion capillary can result in straight lines (often used as criterion for negligible convection in semi-infinite-sample techniques) even in the presence of pronounced convection. Many workers have attempted to detect convective transport contributions by varying the diameter of their diffusion capillary. A plateau in the resulting diffusion coefficient versus capillary diameter is then interpreted as precluding convective masking; see, e.g., [3]. Of course, this conclusion may be erroneous since such a plateau only indicates that the convective effect is diameter-independent. Other workers have proposed the use of magnetic fields to suppress convection during diffusion studies in conducting liquids. Unfortunately, at the very low velocities in question, the magnetic field strength required to achieve "pure" diffusion is so high that, as other work has shown, the diffusion process itself is significantly modified through the Lorentz force acting on the ions and electrons in the liquid [4, 5].

As a consequence of these difficulties, experimental data for self-diffusivities of liquid metals and semimetals obtained with different techniques and/or by different authors

Mail address: J. Iwan D. Alexander, Jean-Francois Ramus, Franz Rosenberger, Center for Microgravity and Materials Research, University of Alabama in Huntsville, Huntsville, Alabama 35899, USA.
Paper submitted: January 3, 1997
Submission of final revised version: January 20, 1997
Paper accepted: February 9, 1997

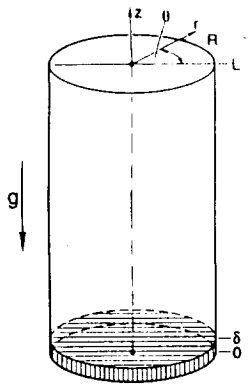

Fig. 1. Model diffusion capillary. Tracer initially located in shaded layer of thickness δ

typically differ by several 10 %, and sometimes by more than 100 % [6, 7]. This is not only an obstacle to realistic process modeling, but to our theoretical understanding of diffusion in liquids as well. Although various theories exist for the diffusion in liquid elements and its temperature dependence, the uncertainties associated with most diffusivity data are too large to allow for an unambiguous evaluation of these theoretical models. Currently, the differences between several theoretical predictions are often less than those between different sets of data for the same system.

To provide quantitative guidance for experimental work, we have numerically modeled diffusive-convective transport in vertical cylinders with dimensions typical for diffusion experiment geometries. To account for thermal convective transport contributions we imposed slight azimuthal temperature asymmetries on the walls and ends of these capillaries. A diffusant, representing the isotopic tracer used in the self-diffusion experiments, is initially located at one end of the capillary. The 3D-time-dependent transport of the diffusant was then simulated for physical properties corresponding to liquid indium. In the following, we present the simulation model, the numerical approach, and the simulation results together with their practical consequences.

2 Simulation Model

The liquid was assumed to be a Boussinesq fluid contained in a closed vertical circular cylinder of length $L = 30$ mm and diameter $2R$ (see fig. 1) of 1 or 3 mm. Gravity acts along the cylinder axis. The temperature on the vertical cylinder wall has the form $T(R, \theta, z) = (T_1 + T_2)/2 + (T_1 - T_2)(\cos(\theta))/2 + \Delta T_z z/L$. Here $T_1 - T_2 = \Delta T_\theta$ is the maximum horizontal temperature difference across the cylinder at any height z, and ΔT_z is the temperature difference between the colder bottom and warmer top faces. The temperatures of these end faces are $T(r, \theta, 0) = (T_1 + T_2)/2 + (T_1 - T_2)r(\cos(\theta))/(2R)$ and $T(r, \theta, L) = T(r, \theta, 0) + \Delta T_z$, respectively. The imposed temperature gradients are time-independent. From this, and their assumed small magnitude, we expect the resulting flow to be steady. Hence, for given values of ΔT_θ, ΔT_z, and R we can compute a steady solution to the following mass, momentum, and heat transport equations:

$$\operatorname{div} \boldsymbol{u} + 0, \tag{1}$$

$$\boldsymbol{u} \cdot \operatorname{grad} \boldsymbol{u} = -\frac{1}{\varrho} \nabla p + \nu \Delta \boldsymbol{u} - \beta(T - T_2)g\boldsymbol{k}, \tag{2}$$

$$\boldsymbol{u} \cdot \operatorname{grad} T = \kappa \Delta T. \tag{3}$$

Here $\boldsymbol{u}$, T, ϱ_0, β, ν, and κ are the liquid's velocity, temperature, density, thermal expansion coefficient, kinematic viscosity, and thermal diffusivity, respectively. Note that, since we consider self-diffusion experiments for which the tracer density is equal to the density of the host liquid, there are no solutal contributions to buoyancy. The no-slip condition for velocity is applied at all walls. Having found the steady velocity and temperature distributions we then use $\boldsymbol{u}$ to compute the evolution of the concentration field $c(\boldsymbol{x}, t)$ from

$$\frac{\partial c}{\partial t} + \boldsymbol{u} \cdot \operatorname{grad} c = D \Delta c, \tag{4}$$

where D is the self-diffusivity. As indicated in fig. 1, the diffusant (tracer) is initially located in a thin layer of thickness δ at one end of the capillary. Hence, the initial concentration distribution is

$$c(z, 0) = c_0, \quad 0 \le z \le \delta \quad \text{and} \quad c(z, 0) = 0, \quad \delta \le z \le L, \tag{5}$$

where $\delta/L \ll 1$. No flux of the tracer is permitted through the walls and ends of the capillary.

The simulations were carried out using the physical properties of molten indium evaluated at $T = 1{,}000$ K (table 1) together with an assumed diffusivity of $1.48 \cdot 10^{-5}$ cm^2/s. Since it is desirable to measure self-diffusion coefficients over a wide temperature range, we have evaluated the relevant properties also at lower temperatures. One sees from table 1 that, in particular, the viscosity varies considerably with temperature. For an extrapolation of our results to lower temperatures, the reader should multiply the $T = 1{,}000$ K value of ΔT_θ by the ratio given in the far right column. For example, at 850 K, the convective contri-

Table 1. Physical properties of indium for different temperatures above the melting point (429 K) calculated from data in [8, 9]. The simulations were carried out for properties corresponding to T = 1,000 K. To obtain the horizontal temperature difference, ΔT_θ, which, at the lower temperatures would give rise to the same flow as the 1,000 K case, multiply the ΔT_θ for 1,000 K by the ratio given in the last column

T [K]	ϱ_0 [g · cm^{-3}]	ν [10^{-3} · cm^2 · s^{-1}]	κ [cm^2 · s^{-1}]	β [10^{-4} · K^{-1}]	$\frac{\Delta T_\theta(T)}{\Delta T_\theta(1{,}000\ \mathrm{K})}$
1,000	6.64	0.78	0.11	1.02	1.0
850	6.74	1.27	0.11	1.01	1.65
600	6.91	2.09	0.11	0.98	2.79
429	7.03	2.65	0.11	0.97	3.60

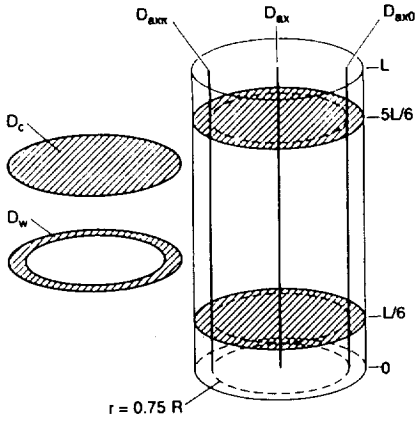

Fig. 2. Defining sketch for data evaluation; for details see text

butions observed at $T = 1{,}000$ K will occur for a ΔT_θ value which is 1.65 times the ΔT_θ at 1,000 K.

The governing equations and boundary conditions for the time-dependent transport of heat, mass, and momentum in the system were solved using finite differences on an equally spaced and a variably spaced mesh using the flow analysis software CFD2000. With the latter method, spatial discretization is achieved using a finite volume technique [10]. The PISO algorithm [11] is used to couple the discretized heat and momentum transport equations which were solved using an ADI method [12]. Owing to the large length to diameter ratio of the capillaries (20 and 60) we found it necessary to employ $24 \times 12 \times 140$ points in the azimuthal, radial, and axial directions, respectively.

3 Data Analysis and Presentation

Time histories of the tracer concentration fields were obtained for different values of R, ΔT_θ, and ΔT_z. To assess the consequences of the different temperature nonuniformities for diffusion coefficient measurements, we treated each of the calculated tracer time histories as we would experimental data. Two approaches were used to deduce diffusivity values from the calculated concentration distributions. In the first approach we employed the method of *Codastefano* et al. [13] in which time records of the concentration $c_1(t)$ and $c_2(t)$, respectively, at the axial sample locations $z = L/6$ and $5L/6$ are used to calculate the diffusivity D from the relation

$$\ln [c_1(t) - c_2(t)] = const. - (\pi/L)^2 Dt. \tag{6}$$

As indicated in fig. 2, the concentration values were taken at the respective positions z as averages over either the entire cross-section ($D = D_C$) or over the ring-shaped region $0.75 \le r \le R$, $0 \le \theta \le 2\pi$ ($D = D_W$).

In the second approach we used the solution to the following 1D diffusion problem for $c(z, t)$

$$\frac{\partial c}{\partial t} = D \frac{\partial^2 c}{\partial z^2}, \tag{7}$$

$$\frac{\partial c(0, t)}{\partial z} = 0, \quad t \ge 0, \tag{8}$$

$$c(z, 0) = c_0, \quad 0 \le z \le \delta, \quad \text{and} \quad c(z, 0) = 0, \quad \delta \le z \le L, \tag{9}$$

where $\delta \ll L$ and $c(z, t)$ is bounded as $z \to \infty$. The solution has the form [14]

$$c(z, t) = \frac{c_0}{\sqrt{\pi D t}} \exp\left(\frac{-z^2}{4Dt}\right), \tag{10}$$

and D is obtained graphically from the slope m of $\ln (c(z, t))$ versus z^2 at $t = t^*$, where m is given by

$$m = \frac{\partial \ln (c(z, t^*))}{\partial z^2} = \frac{-1}{4Dt^*}. \tag{11}$$

In the second method we calculated three diffusivities from the concentration profiles along the three vertical axes represented by heavy lines in fig. 2. One value was obtained from the axial concentration profile at $r = 0$ ($D = D_{ax}$) and the other two from axial profiles taken at $r = 0.75R$ and $\theta = 0$ and π ($D = D_{ax0}$, $D = D_{ax\pi}$) respectively.

4 Results and Discussion

The results of our simulations are summarized in table 2. One sees that, irrespective of the application of a "stabilizing" ΔT_z, with the 1 mm diameter capillary the horizontal temperature difference ΔT_θ must not exceed 0.1 K for the apparent diffusivity D to be within a few percent of the actual (input) diffusivity D_0. However, at $\Delta T_\theta = 1$ K, which we consider as a readily occurring temperature nonuniformity for experiments at 1,000 K, D_C exceeds D_0 by over 100 %. The magnitude of this convective contamination, though somewhat reduced by the ΔT_z of 2 K, fully demonstrates the difficulty of accurately measuring diffusivities at elevated temperatures in the presence of gravity. These results are further illustrated in fig. 3a with time records for c_1 and c_2 used in the Codastefano method, eq. (6). The convective transport contributions become particularly apparent when comparing the curves obtained with gravity (heavy solid lines: $\Delta T_z = 0$, dashed lines: $\Delta T_z = 2$ K) with the thin solid line resulting under purely diffusive conditions. On the other hand, the plots of $\ln (c_1 - c_2)$, obtained under these strongly contaminated conditions, are as straight as one would expect for pure diffusion. Thus, the straight line character of these plots cannot be used as a

*Table 2. Apparent diffusivities in units of [10^{-5} cm^2 s^{-1}] obtained from the simulations with input diffusivity $D_0 = 1.48 \cdot 10^{-5}$ cm^2 s^{-1}. Values with * obtained at $t = 300$ min, with ** at 356 min*

$\Delta T_z = 0$ K	$2R = 1$ mm			$2R = 3$ mm		
ΔT_θ [K]	1.0	0.1	0.01	0.1	0.05	0.01
D_C	3.69	1.50	1.48	7.92	3.08	1.54
D_W	3.69	1.50	1.48	7.92	3.08	1.54
D_{ax}	2.25**	1.50*	1.51**	7.87**	3.26*	1.60*
D_{ax0}	2.25**	1.49*	1.49**	6.18**	2.75*	1.51*
$D_{ax\pi}$	2.25**	1.49*	1.49**	8.43**	3.45*	1.57*
$\Delta T_z = 2$ K						
ΔT_θ [K]	1.0	0.1		0.1	0.077	0.01
D_C	2.63	1.51*	–	8.93	5.73	1.55
D_W	2.63	1.51*	–	8.93	5.73	1.57
D_{ax}	2.25**	1.48*	–	8.76**	7.02*	1.60*
D_{ax0}	2.25**	1.47*	–	7.19**	5.96*	1.51*
$D_{ax\pi}$	2.25**	1.47*	–	8.76**	7.64*	1.57*

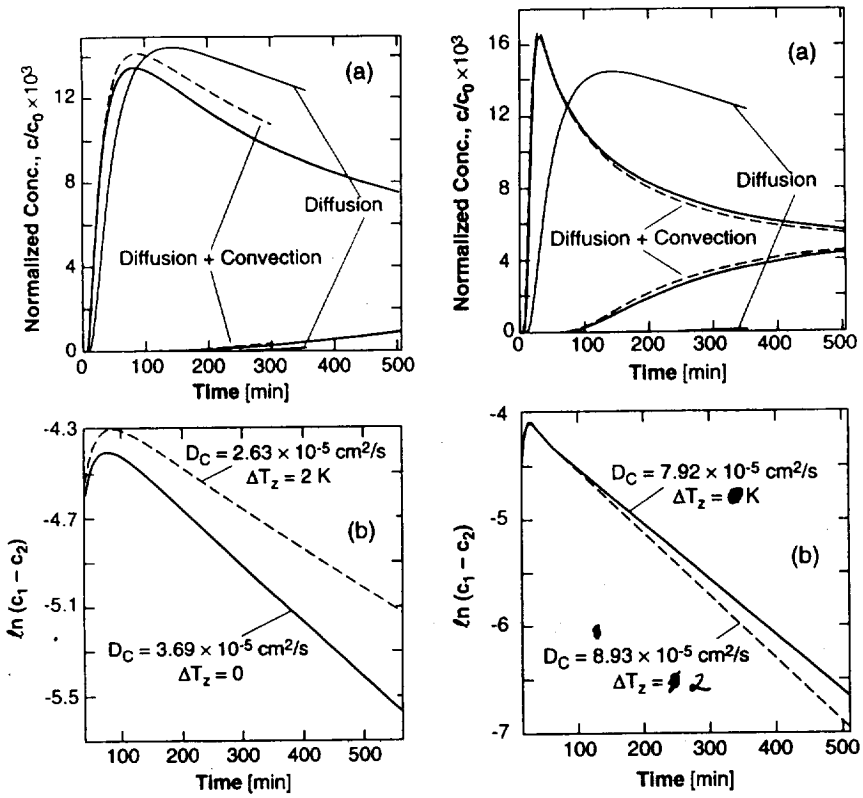

Fig. 3 (left). (a) Normalized average concentration c_1 (upper curves) and c_2 (lower curves) vs time and (b) ln $(c_1 - c_2)$ vs time, for $2R = 1$ mm and $\Delta T_0 = 1$ K. The pure diffusion case is shown for reference in (a). The solid and dashed lines correspond to $\Delta T_z = 0$ and 2 K, respectively

Fig. 5. (right). (a) Normalized average concentration c_1 (upper curves) and c_2 (lower curves) vs time and (b) ln $(c_1 - c_2)$ vs time, for $2R = 3$ mm and $\Delta T_0 = 0.1$ K. The pure diffusion case is shown for reference in (a). The solid and dashed lines correspond to $\Delta T_z = 0$ and 2 K, respectively.

criterion for the absence of significant convective contributions. More insight on the convective mixing in this case can be obtained from the isoconcentration lines in the plane $\theta = 0, \pi$ (fig. 4). The deformation of these lines, which under purely diffusive conditions would be strictly straight and horizontal reflects a convection role with the liquid rising at the right ("hotter") wall and sinking at the left wall. Characteristic convection velocities associated with these rolls are of the order of $8 \cdot 10^{-4}$ cm/s. A comparison of these concentration contours for $\Delta T_z = 0$ (solid line) and $\Delta T_z = 2$ K (dashed lines) again illustrates the limited effect of the common practice to keep the top of the diffusion capillary somewhat warmer in order to suppress convection.

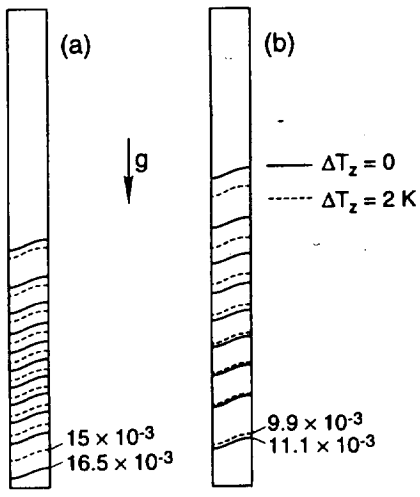

Fig. 4. Normalized concentration contours for $2R = 1$ mm and $\Delta T_0 = 1$ K at (a) $t = 178$ and (b) 356 min. Contour intervals: (a) $5 \cdot 10^{-4}$; (b) $4 \cdot 10^{-4}$

The results for 3 mm diameter capillaries are even more sobering. Table 2 reveals that ΔT_θ's of a few 10^{-2} K suffice to induce intolerable convection contamination. For the case of $\Delta T_\theta = 0.1$ K, the strong convective contributions become apparent by comparing the plots of c_1 and c_2 in fig. 5a with those in fig. 3a. One sees that in the wider capillary the concentration at the "Codastefano locations" (see above) increases much more rapidly than in the narrower capillary. This is due to an increase of the convective velocities to $7 \cdot 10^{-3}$ cm/s. This increase is also reflected in the stronger deformation of the isoconcentration lines, which are presented in fig. 6 for this case. In spite of this heavy convective contamination, the linearity of the ln $(c_1 - c_2)$ versus time curves at large times (fig. 5b) might again lead one to erroneously conclude that convection is insignificant! Equally interesting is the result that $\Delta T_z = 2$ K, rather than reducing the flow induced by ΔT_θ, slightly enhances the convective contribution. We have observed a similar behavior associated with transport during Bridgman–Stockbarger solidification under microgravity conditions [15].

The above discussion was restricted to D-values obtained by the Codastefano method, eq. (6). The apparent diffusivities obtained by the second method, eq. (10), reflect a similar behavior. Despite the obvious convective contaminations, plots of the logarithm of the concentration versus the square of the distance along the diffusion capillary (which are employed in this method for D-evaluations, see

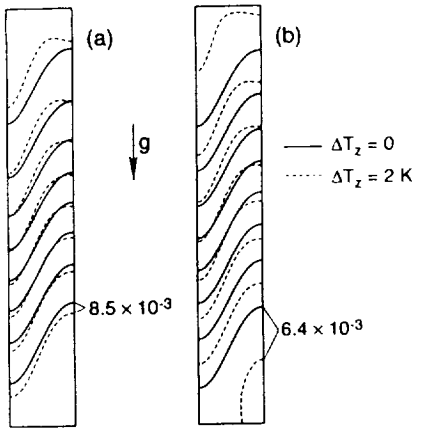

Fig. 6. Normalized concentration contours for $2R = 3$ mm and $\Delta T_0 = 0.1$ K at (a) $t = 178$ and (b) 356 min. Contour intervals: (a) 10^{-3}; (b) $4 \cdot 10^{-4}$

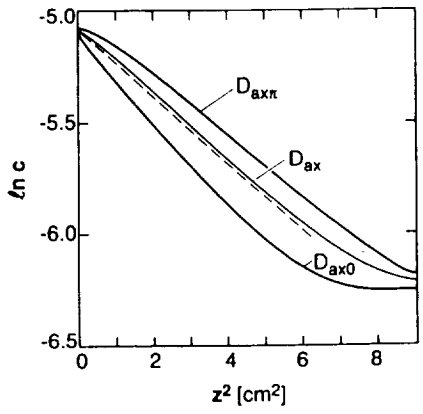

Fig. 7. Plots of ln c vs z^2 along the three axis defined in fig. 2. Same sample as in figs. 3 and 4: $2R = 1$ mm and $\Delta T_0 = 1$ K, $\Delta T_z = 0$, at $t = 356$ min. Dashed straight line: guide for the eye to emphasize absence of curvature in profiles over large parts of the sample

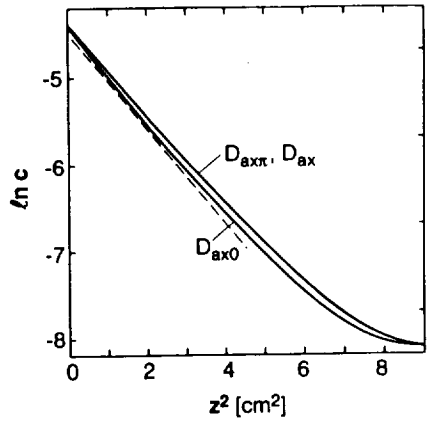

Fig. 8. Plots as fig. 7 samples as in figs. 5 and 6: $2R = 3$ mm and $\Delta T_0 = 0.1$ K, $\Delta T_z = 0$, at $t = 356$ min

eq. (11)) result in rather straight lines over major portions of the sample. This is depicted in figs. 7 and 8, respectively, for the $\Delta T_z = 0$ cases of figs. 3 and 5. Typical liquid diffusivity studies involve the solidification of the sample before the chemical analysis for $c(z)$ determination. This solidification often results in high porosity or deformation of the last part of the sample to freeze. On discarding this part of the sample, an investigator would again reach the erroneous conclusion that convective contamination was insignificant.

5 Summary and Conclusion

We found that temperature nonuniformities of magnitudes that, in particular at high temperatures, are practically unavoidable during diffusivity measurements in liquids, cause strong convective contamination of the diffusivity data. Furthermore, the convective contribution to transport is only insignificantly reduced by a "stabilizing" ΔT_z. Hence, the widely used approach of keeping the top of diffusion samples slightly warmer than the bottom appears to be a dubious means of "preventing convection". Most strikingly, we found that diffusive-convective transport can result in temporal local concentration changes and axial concentration profiles that are analytically indistinguishable from pure diffusion profiles. This finding casts considerable doubt on various geometrical criteria previously used to demonstrate the absence of significant convective contamination in diffusivity data plots.

From this study we conclude that reduced gravity conditions are essential for definitive diffusivity measurements in liquid phases of macroscopic dimensions.

Acknowledgments

This work has been supported by the Microgravity Science and Application Division of the National Aeronautics and Space Administration under contract NAS8-39716 and grant NCC8-99, and by the State of Alabama through the Alabama Supercomputer Network and the Center for Microgravity and Materials Research at the University of Alabama in Huntsville.

References

1 *Verhoeven, J. D.:* Convection Effects in the Capillary Reservoir Technique for Measuring Liquid Metal Diffusion Coefficients. Trans. Met. Soc. AIME, vol. 242, p. 1937 (1968)
2 *Persson, T., Erikson, P. E., Linström, L.:* Convection and Other Disturbing Effects in Diffusion Experiments in Liquid Metals. J. Physique, vol. 41, p. C8-374 (1980)
3 *Careri, G., Paoletti, A. and Salvetti, F.:* Self-diffusion in Liquid Indium. Nuovo Cimento, vol. 10, p. 399 (1954)
4 *Youdelis, W. V., Colton, D. R., Cahoon, J. R.:* On the Theory of Diffusion in a Magnetic Field. Can. J. Phys., vol. 42, p. 2217 (1964)
5 *Youdelis, W. V., Colton, D. R., Cahoon, J. R.:* Diffusion in a Magnetic Field. Can. J. Phys., vol. 48, p. 805 (1970)
6 *Shimoji, M., Itami, T.:* Atomic Transport in Liquid Metals. Trans. Tech. Publ., Aedermannsdorf, Switzerland (1986)
7 *March, N. H.:* Liquid Metals – Concepts and Theory. Cambridge Univ. Press, Cambridge (1990)
8 *Ida, T., Guthrie, R. I. L.:* The Physical Properties of Liquid Metals. Clarendon, Oxford (1988)
9 *Lind, M. D.:* Thermocapillary Flows and Float Zone Processes. AIAA-Paper 87-0618, 25th Aerospace Sciences Meeting, Reno NV (1987)
10 *Patankar, S. V.:* Numerical Heat Transfer and Fluid Flow. Series in Computational Methods in Applied Mechanics and Thermal Sciences, Hemisphere, London (1980)
11 *Issa, R. I.:* Solution of the Implicit Discretized Fluid Flow Equations by Operator Splitting. J. Comput. Phys., vol. 62, p. 40 (1985)
12 *Birkhof, G., Lynch, R.:* Numerical Solution of Elliptic Problems. SIAM Studies in Applied Mathematics (1984)
13 *Codastefano, P., Di Russo, A., Zanza, V.:* New Apparatus for Accurate Diffusion Measurements in Fluids. Rev. Sci. Instr., vol. 48, p. 1650 (1977)
14 *Crank, J.:* The Mathematics of Diffusion. Clarendon Press, Oxford, p. 13 (1975)
15 *Alexander, J. I. D., Ouazzani, J., Rosenberger, F.:* Analysis of the Low Gravity Tolerance of Bridgman–Stockbarger Crystal Growth. J. Crystal Growth, vol. 97, p. 285 (1989)